

Reconstructing the pyrite deformation mechanism map

Craig D. Barrie^{1+*} Mark A. Pearce² and Alan P. Boyle³

¹NERC Isotope Community Support Facility, Scottish Universities Environmental Research Centre, Scottish Enterprise Technology Park, Rankine Avenue, East Kilbride, Glasgow, G75 0QF

²Geospatial Research Ltd., Department of Earth Sciences, University of Durham, Durham, DH1 3LE

³Department of Earth and Ocean Sciences, University of Liverpool, Liverpool, L69 3GP

ABSTRACT

Deformation mechanism maps are important tools to understand how minerals deform across a range of pressure, temperature and strain rate conditions. Recent studies have suggested that the current deformation mechanism map for pyrite is in need of revision, with plastic deformation evident over a much wider range of conditions than it proposes. This study uses stress-strain data from experimentally deformed pyrite, combined with electron backscatter diffraction (EBSD) results from a range of experimental and natural samples to construct a revised pyrite deformation mechanism map. This map corresponds to polycrystalline pyrite with a grain size of $\sim 35\mu\text{m}$ and suggests the onset of crystal plasticity at geological strain rates ($\sim 10^{-12}$ - 10^{-16} s^{-1}) occurs at temperatures as low as $\sim 260 \text{ }^\circ\text{C}$. The revised mechanism map is based upon all available data, experimental data for pyrite are limited and acquired at geologically unreasonable, fast strain rates (10^{-4} -

* Email: craig.barrie@glasgow.ac.uk

10⁻⁵ s⁻¹), and strain rates for the naturally deformed samples can only be estimated. Therefore, considerable extrapolation is required and while this revised map is an improvement upon the existing map, it should still only be considered a 'guide' to the potential deformation mechanisms, which may operate across a range of P-T conditions in polycrystalline pyrite-rich ores.

Keywords: pyrite, deformation mechanism map, experimental deformation, natural deformation, EBSD

1. Introduction

Pyrite (FeS₂) is the most abundant sulphide mineral in the Earth's crust and occurs in a myriad of environments, but is ubiquitous in sulphide ore deposits (Mann et al. 1990; Gu and McClay 1992; Brown and McClay 1993; Craig and Vokes 1993; Cook 1996; Craig et al. 1998). Many ore deposits form on or close to the seafloor at rifted margins and, therefore, at some stage in their history become involved in orogenic events, experiencing deformation and/or metamorphism (Vokes, 1980; Allen et al., 2002). Pyrite itself is not of economic importance, but its refractory nature allows it to resist the remobilisation and recrystallisation processes that commonly affect the softer, economic sulphides such as sphalerite, galena and chalcopyrite during retrogression, enabling it to preserve evidence of preceding high temperature events (McClay and Ellis 1983; Marshall and Gilligan 1987; Plimer 1987; Marshall and Gilligan 1993; Bailie and Reid 2005). Understanding the deformation mechanisms that operate in pyrite across different P-T conditions is, therefore, essential in reconstructing the post-depositional history of ore deposits and maximising their exploitation (Freitag et al., 2004).

1
2
3
4
5
6
7
8
9
10
11
12
13
14
15
16
17
18
19
20
21
22
23
24
25
26
27
28
29
30
31
32
33
34
35
36
37
38
39
40
41
42
43
44
45
46
47
48
49
50
51
52
53
54
55
56
57
58
59
60
61
62
63
64
65

Pyrite deformation mechanisms have been the focus of a number of studies since the early 1960s, initially using experimental deformation, reflected light analysis and etching to reveal dislocation microstructures (Gill 1969; Ramdohr 1969; Graf and Skinner 1970; Atkinson 1975). All of this work suggested pyrite was a hard mineral, which deformed by brittle mechanisms at all levels in the Earth's crust. Subsequent high resolution transmission electron microscopy (HR-TEM) of experimentally deformed pyrite revealed the presence of dislocations within pyrite grains suggesting crystal-plastic deformation could operate at temperatures as low as ~425 °C (Couderc et al., 1980; Cox et al., 1981; Graf et al., 1981; Levade et al., 1982). These experimental results were combined with analysis of naturally deformed pyrite to construct the current pyrite deformation mechanism map (McClay and Ellis, 1983) (Fig. 1).

FIG. 1 HERE

Deformation mechanism maps are graphical models that show the dominant deformation mechanism for a given mineral at different conditions (Ashby, 1972; Frost and Ashby, 1982). These maps assist understanding of the general conditions under which deformation mechanisms operate and are available for a number of minerals (quartz, calcite, galena, etc) (e.g. White 1976; Atkinson 1977; Frost and Ashby 1982; Ranalli 1982; Tsenn and Carter 1987; Drury and Humphreys 1989). Whilst the field name denotes the dominant mechanism, this mechanism is not exclusive and other subordinate mechanisms may also be active (Mohamed and Langdon, 1974; Pearce and

1 Wheeler, In Press). Deformation mechanism maps need to be used with
2 caution, partly because of the limited data on the high temperature operation
3 of various mechanisms and also because construction requires significant
4 extrapolation from experimental to geological strain rates (Rutter, 1976;
5 White, 1976; Cox, 1987; Siemes, 1991).
6
7
8
9
10

11
12 Recent studies of deformed pyrite using electron backscatter diffraction
13 (EBSD) have indicated the pyrite deformation mechanism map of McClay and
14 Ellis (1983) (Fig. 1) needs revision. Results from these studies reveal crystal-
15 plastic deformation operates in pyrite over a much wider range of P-T, grain
16 size and strain rate conditions than previously suggested and potentially at
17 temperatures as low as ~200 °C (Barrie et al., 2007; Barrie et al., 2009; Barrie
18 et al., 2010a). Combining the results of these previous findings with
19 assessment of further experimental samples this study has three principal
20 aims:
21
22
23
24
25
26
27
28
29
30
31
32

- 33
34
35
36 1. To determine how deformation mechanisms in pyrite vary across a
37 range of well-constrained temperature, stress and strain rate conditions
38 from experimentally deformed samples and how they compare with
39 results from naturally deformed samples.
40
41
42
43
44
45
46
47
- 48 2. To understand how cataclastic textures and recovery/recrystallisation
49 processes affect the ability to detect crystal-plastic deformation in pyrite.
50
51
52
53
54
- 55 3. To use the results gathered from this, and earlier studies of both natural
56 and experimentally deformed pyrite to construct a new pyrite
57
58
59
60
61

1 deformation mechanism map, outlining the problems and opportunities
2 of this revised map.
3
4
5
6

7 **2. Methodology**

8
9 The samples discussed in this study have all been prepared and
10 analysed using the same techniques as those of Barrie et al. (2007).
11
12 Therefore, only a brief description of sample preparation and data analysis is
13
14
15
16
17 given below.
18
19
20

21 TABLE 1 HERE
22
23
24
25

26 **2.1. Samples**

27
28 All of the experimentally deformed samples discussed in this study
29 (Table 1) come from an original block of fine grained polycrystalline pyrite-rich
30 ore from the Blow ore body of the Mt Lyell Mining and Railway Company near
31 Queenstown, Tasmania (Cox et al., 1981; Barrie et al., 2007). Suites of the
32
33
34
35
36
37
38
39
40
41
42
43
44
45
46
47
48
49
50
51
52
53
54
55
56
57
58
59
60
61
62
63
64
65

62 naturally deformed samples included in this study are from polymetallic,

1 pyrite-rich ore deposits and were previously discussed by Barrie et al. (2009;
2 2010a).
3
4
5
6

7 FIG. 2 HERE
8
9

10 11 **2.2. Electron backscatter diffraction (EBSD)**

12 All pyrite crystallographic orientation data were collected by EBSD at the
13 University of Liverpool using a CamScan X500 crystal probe scanning
14 electron microscopes (SEM). The CamScan X500 is equipped with a
15 thermionic field emission gun and was used with an accelerating voltage of
16 20kV and a beam current of ~5nA during analysis. Electron backscatter
17 patterns were collected on a phosphor screen and processed using the
18 software package CHANNEL 5 service pack 6 (*Oxford Instruments Ltd*). The
19 angular resolution of this technique is typically better than $\sim 1^\circ$ with a spatial
20 resolution of $\sim 0.05\mu\text{m}$ (Prior et al., 1999; Wheeler et al., 2001; Ohfuji et al.,
21 2005). All of the samples, prior to analysis, were polished on a polyurethane
22 lap for $\sim 2\text{h}$ using a suspension of $0.05\mu\text{m}$ colloidal silicon (SYTONTM) to
23 remove any surface damage. Samples were also given a thin carbon coat
24 ($\sim 4\text{-}6\text{nm}$), prior to EBSD, in order to reduce charging effects and maintain a
25 strong crystallographic signal (Prior et al., 1996; Prior et al., 1999). Following
26 acquisition the data were post-processed to remove noise and interpolate a
27 small number of missing points using routines outlined by Barrie et al. (2007).
28
29
30
31
32
33
34
35
36
37
38
39
40
41
42
43
44
45
46
47
48
49
50
51
52
53
54
55

56 **2.3. Orientation Contrast Imaging and Band Contrast Mapping**

57 Forescatter orientation contrast (OC) images were utilised throughout
58
59
60
61
62
63
64
65

1 this study and are generated by detectors in an SEM positioned in front of
2 samples (Prior *et al.*, 1999). These images reveal misorientation of the crystal
3 lattice of individual grains through grey scale variation. Where grains are
4 undeformed they will appear homogeneous in OC images. If, however,
5 deformation has occurred then the grain will contain grey scale variation as a
6 result of lattice misorientation (for further details see Prior *et al.*, 1996, 1999).
7
8
9
10
11
12
13

14 Band contrast maps are generated during EBSD and are indicative of
15 diffraction pattern quality, with grey-scale differences representing the quality
16 of the diffraction pattern at individual points (Bestmann and Prior, 2003; Prior
17 *et al.*, 2002). The quality of the diffraction patterns is a function of a number of
18 factors but largely represents the quality of the lattice so that pristine crystal
19 lattice is bright whilst distorted lattice with abundant dislocations is darker,
20 Grain boundaries and fractures do not return any patterns so appear black
21 meaning that band contrast images give a good picture of the rock
22 microstructure. Band contrast maps are used throughout this study to
23 highlight changes in pyrite microtextures, with increasing temperature of
24 deformation (Barrie *et al.*, 2007), which are beyond the resolution of SEM
25 imaging.
26
27
28
29
30
31
32
33
34
35
36
37
38
39
40
41
42
43

44 To quantify the amount of lattice distortion within a sample, the mean
45 misorientation was calculated for each grain. This is the sum of the
46 misorientation between each pixel of a grain and the mean orientation of that
47 grain divided by the number of pixels and therefore is analogous to the
48 variance of the orientations within a grain. These mean misorientations are
49 then averaged over the whole sample to give an average mean misorientation
50 for each sample.
51
52
53
54
55
56
57
58
59
60
61
62
63
64
65

3. Results

Detailed results for the naturally deformed samples discussed in this study are presented elsewhere (Barrie et al., 2009; Barrie et al., 2010a) as are those for one suite of the experimental samples (Barrie et al., 2007). Therefore, only the characteristics of the experimental samples new to this study will be outlined. Siemes et al. (1993) and Barrie et al. (2007) described the starting material, from which all of the experimental samples were deformed, and their results are included in this study to assist with textural, grain size and grain-distortion comparisons (Fig. 3, 4A).

FIG. 3 HERE

FIG. 4 HERE

3.1. Low-Temperature Experimental Runs (450-500 °C)

Three samples were deformed at temperatures between ~450-500 °C (Table 1; Fig. 2) and strain rates of $2 \times 10^{-4} \text{ s}^{-1}$ (run 049) and $2 \times 10^{-5} \text{ s}^{-1}$ (runs 032 and 035). All of these runs failed prior to completion and preserve evidence for brittle textures (Fig. 5). Fracturing is widespread in run 032 (450 °C) where conjugate shear zones have developed at $\sim 45^\circ$ to shortening (Fig. 5A, B). Pyrite grains within these zones contain sharp, irregular boundaries and grain size is $\sim 10\text{-}20\mu\text{m}$ (Fig. 5C), while pyrite grains outside these zones are equant and $\sim 35\text{-}40\mu\text{m}$ in size (Fig. 3, 5D). Runs 049 (470 °C) and 035 (500 °C) have less extensive fracturing, and are characterised by equant pyrite grains with relatively straight, often bulged grain boundaries (Fig. 4B, C). While all of the samples contain a similar, mean grain size of $\sim 35\text{-}40\mu\text{m}$

1 (Fig. 3A), Runs 049 and 035 do contain suites of <10µm, rounded pyrite
2 grains surrounding larger pyrite grains (Fig. 3B, C, 4B, C).
3

4
5 Orientation contrast (OC) images show lattice orientation varying within
6 pyrite grains in all three of the low temperature runs. EBSD results indicate
7 cumulative lattice distortion (Fig. 6A, B) within pyrite grains and the
8 development of low-angle (~2°) sub-grain boundaries, although this is rare at
9 450 °C (032). The average mean misorientation within pyrite grains at 450 °C
10 is ~2° (Fig. 6B), while results for the 470-500 °C samples are larger ~4-5°
11 (Fig. 6A, B). Neighbour-pair misorientation histograms (Wheeler et al., 2001)
12 reveal low-angle (~2°) peaks within all of these runs with the peak height
13 increasing with temperature (Fig. 7).
14
15
16
17
18
19
20
21
22
23
24
25
26
27
28

29 FIG. 5 HERE
30
31
32
33

34 **3.2. Mid-Temperature Experimental Runs (550-600°C)**

35
36 Six samples were deformed at temperatures between 550-600 °C and
37 strain rates of $2 \times 10^{-4} \text{ s}^{-1}$ (runs 048, 063, 092), $2 \times 10^{-5} \text{ s}^{-1}$ (runs 037, 054) 1.2
38 $\times 10^{-1} \text{ s}^{-1}$ (run 026) (Table 1; Fig. 2). All of the 550-600 °C samples show
39 similar textural characteristics. Although four of the runs terminated with
40 specimen failure (Fig. 2), fracturing appears minimal. Mean grain size within
41 all of the runs is ~35-40µm (Fig 3A) with only 092 having a larger grain size,
42 possibly due to the starting material being cored from a coarser layer of the
43 original ore (Barrie et al., 2007; Cox et al., 1981). Pyrite grain boundaries tend
44 to be sutured and decorated by small (<10µm), anhedral pyrite grains (Fig.
45 4D, E).
46
47
48
49
50
51
52
53
54
55
56
57
58
59
60
61
62
63
64
65

1 OC images indicate widespread internal grey-scale variation within pyrite
2 grains in all of the samples (Fig. 8A, C). EBSD results reveal widespread and
3 abundant low-angle ($\sim 2^\circ$) low-angle sub-grain boundaries within most if not all
4 pyrite grains (Fig. 8B, D) with a maximum mean misorientation of $\sim 12^\circ$ and an
5 average across the samples of $\sim 4\text{-}5^\circ$ (Fig. 6). Neighbour-pair misorientation
6 histograms reveal a low-angle ($\sim 2^\circ$) peak for the $2 \times 10^{-5} \text{ s}^{-1}$ 550 °C run (037),
7 which decreases in intensity at higher temperature (for the same strain rate,
8 sample 054). (Fig. 7).
9
10
11
12
13
14
15
16
17
18
19
20

21 FIG. 6 HERE

22
23 FIG. 7 HERE
24
25
26
27
28

29 **3.3. High-Temperature Experimental Runs (650-700°C)**

30 Six samples were deformed at temperatures between 650-700 °C and
31 strain rates of $2 \times 10^{-4} \text{ s}^{-1}$ and $2 \times 10^{-5} \text{ s}^{-1}$ (Table 1; Fig. 2). All of the runs have a
32 mean grain size of $\sim 35\text{-}40\mu\text{m}$ (Fig. 3A) with the exception of run 020, which
33 has notably larger ($\sim 45\mu\text{m}$) grain size, most probably reflecting a coarser
34 layer of the original starting material. None of the runs within this temperature
35 regime failed during deformation and there is minimal evidence for fracture
36 development. Pyrite grain boundaries in the 650 °C samples at $2 \times 10^{-4} \text{ s}^{-1}$ are
37 sutured and many preserve elongate or 'ribbon' like textures, often decorated
38 by suites of smaller anhedral pyrite grains ($<20 \mu\text{m}$). Pyrite grains deformed at
39 650 °C, and 700 °C in the $2 \times 10^{-5} \text{ s}^{-1}$ samples, have long, curved pyrite-pyrite
40 grain boundaries often lobate (Fig. 4F) but not sutured.
41
42
43
44
45
46
47
48
49
50
51
52
53
54
55
56
57
58
59
60
61
62
63
64
65

1 OC images indicate internal grey-scale variation is present within some
2 pyrite grains, but the majority appear homogeneous (Fig. 8E, G). Low-angle
3 (~2°) sub-grain boundaries are present within some pyrite grains, but are not
4 widespread. They are generally restricted to grain boundaries and rarely
5 within grain cores (Fig. 8F, H). Mean misorientation within pyrite grains is
6 relatively low with a maximum of ~6° at 650 °C and ~4° at 700 °C (Fig. 6). The
7 low-angle (~2°) boundary peak in the neighbour-pair misorientation
8 histograms for the $2 \times 10^{-5} \text{ s}^{-1}$ runs at both 650 °C (055) and 700 °C (020) are
9 of a similar height to the low-angle peak in the starting material (B-1) (Fig. 7).

10
11
12
13
14
15
16
17
18
19
20
21
22
23
24 FIG. 8 HERE

25 26 27 28 **4. Discussion**

29 30 **4.1. Brittle Vs Crystal-Plastic Deformation**

31
32
33
34 Brittle deformation textures are only evident in the lowest temperature
35 runs (<500 °C), with conjugate shear zones developed at 450 °C (032) (Fig.
36 5A, B, C). However, while brittle mechanisms are clearly evident at 450 °C
37 (032), OC imaging and EBSD analysis indicates lattice distortion is present in
38 the pyrite grains surrounding the shear zones and unaffected by cataclasis
39 (Fig. 5A, B). This distortion implies at least some crystal-plastic deformation
40 has operated in these samples, although subordinate to the dominantly brittle
41 behaviour. These results suggest that temperatures of ~450 °C may represent
42 the transition zone between cataclastic and crystal-plastic mechanisms of
43 deformation at fast strain rates of 10^{-4} s^{-1} - 10^{-5} s^{-1} (Fig. 2, 5). Brittle behaviour
44 is also apparent in the runs deformed at >500 °C, however, it is minimal and
45
46
47
48
49
50
51
52
53
54
55
56
57
58
59
60
61
62
63
64
65

1 most, if not all, pyrite grains are internally dominated by dislocation-wall
2 formation and thus, crystal-plastic deformation (Fig. 8).
3

4 Similarly, naturally deformed pyrite-rich ores that have experienced
5 metamorphism and/or deformation are often characterised by brittle textures
6 of deformation (Marshall and Gilligan, 1987; Cook, 1993; Cook et al., 1993;
7 Craig and Vokes, 1993; Cook, 1995; Craig, 2001; Kuscu and Erler, 2002).
8 Most of these studies consider such textures as evidence that pyrite has
9 behaved in a brittle manner at peak metamorphic conditions. However, these
10 assumptions, based primarily upon reflected light analysis and BSE imaging,
11 can be misleading as the techniques reveal nothing about internal distortion in
12 pyrite grains. Instead, the eye is drawn to the most prevalent visible
13 deformation texture, which did not necessarily operate at peak conditions.
14
15
16
17
18
19
20
21
22
23
24
25
26
27

28 Pyrite from the Bleikvassli (Cook, 1993) and Rødhammeren (Nilsen,
29 1971) sulphide ore deposits, in the Scandinavian Caledonides, are
30 characterised by cataclasis and 'pulverisation'. However, when investigated
31 by OC imaging and EBSD, regardless of the prevalence of brittle textures, the
32 pyrite preserves evidence for widespread internal crystal-plastic distortion
33 (Barrie et al., 2010a). These results, coupled with those from similar studies
34 (Boyle et al., 1998; Freitag et al., 2004; Barrie et al., 2009; Barrie et al.,
35 2010b), imply brittle textures in naturally deformed pyrite are generally not
36 indicative of peak metamorphism, but most likely represent textures formed
37 during later overprinting retrograde conditions of metamorphism.
38
39
40
41
42
43
44
45
46
47
48
49
50
51
52

53 Recent study of low temperature deformed ore deposits (Barrie et al.,
54 2009) indicate that crystal-plastic deformation in naturally deformed pyrite (10^{-12}
55 – 10^{-16} s⁻¹) potentially occurs at temperatures as low as ~200-260 °C, far
56
57
58
59
60
61
62
63
64
65

1
2
3
4
5
6
7
8
9
10
11
12
13
14
15
16
17
18
19
20
21
22
23
24
25
26
27
28
29
30
31
32
33
34
35
36
37
38
39
40
41
42
43
44
45
46
47
48
49
50
51
52
53
54
55
56
57
58
59
60
61
62
63
64
65

lower than suggested by the current pyrite deformation mechanism map (Fig. 1) (McClay and Ellis, 1983).

4.2. Recovery and Recrystallisation Processes

Plastic mechanisms of deformation are often associated with recovery and/or recrystallisation processes (McClay and Ellis, 1983; Urai et al., 1986; Leiss and Barber, 1999). These processes either encourage ordering of dislocations within grains to form low-angle ($\sim 2^\circ$) dislocation walls/sub-grain boundaries (recovery) or remove dislocations from grains (recrystallisation). Textural evidence for recrystallisation within naturally deformed pyrite is uncommon (Barrie et al., 2010a; Barrie et al., 2010b), potentially due to a combination of 'softer' matrix sulphide effects favouring grain boundary sliding (GBS) processes over recrystallisation, slow strain rates ($10^{-12} - 10^{-16} \text{ s}^{-1}$) and 'relatively' low temperatures of deformation.

In contrast to naturally deformed samples, the majority of experimental runs discussed in this study and by Barrie et al. (2007) preserve evidence for widespread recrystallisation (Fig. 4). The runs deformed at a strain rate of $2 \times 10^{-4} \text{ s}^{-1}$ and 550-700 °C (Fig. 2B) preserve evidence for recrystallisation processes that systematically alter from bulging (BLG) recrystallisation to sub-grain rotation (SGR) and grain boundary migration (GBM) with increasing temperature (Hirth and Tullis, 1992; Barrie et al., 2007). The experimental samples described in this study cover a greater range of temperature and strain rate conditions than Barrie et al. (2007), thus allowing further assessment of recrystallisation processes at fast strain rates (Table 1; Fig 2). The lowest temperature run, 032 (450 °C), contains no evidence for formation

1 of new, recrystallised grains, and retains pyrite grain size and shape, outside
2 shear zones (Fig 5), similar to the starting material (B-1) (Fig. 4). However,
3
4 the 470 °C and 500 °C runs (Fig. 4) preserve microstructures similar to those
5
6 in samples deformed at 550 °C in Barrie et al. (2007), with suites of
7
8 recrystallised, anhedral pyrite grains (<5µm) decorating the boundaries of
9
10 remnant 'porphyroclastic' pyrite grains (Fig. 4). These textures, as well as
11
12 apparent suturing along 'porphyroclastic' grain boundaries (Fig. 4B, C)
13
14 suggest the onset of recrystallisation processes in pyrite, at fast strain rates
15
16 (10^{-4} s^{-1} - 10^{-5} s^{-1}), occurs at ~470-500 °C and is initially dominated by BLG
17
18 recrystallisation.
19
20
21
22
23

24 At a strain rate of $2 \times 10^{-5} \text{ s}^{-1}$ and temperatures between 550-600 °C, the
25
26 runs preserve a recrystallisation trend similar to that of Barrie et al., (2007),
27
28 with BLG becoming replaced by SGR recrystallisation (Fig. 4). However, at
29
30 650 °C and $2 \times 10^{-5} \text{ s}^{-1}$ (055) (Table 1, Fig. 4) GBM recrystallisation processes
31
32 appear to dominate rather than SGR (Barrie et al., 2007). However, 055 not
33
34 only experienced a different strain rate to the 650 °C sample (059) discussed
35
36 in Barrie et al, (2007) but also a much lower total strain ~15% compared to
37
38 ~40% (Table 1; Fig. 2). This suggests relatively high deformation
39
40 temperatures and low total strains potentially favour GBM over SGR
41
42 recrystallisation. Despite these differences, the results imply recrystallisation
43
44 processes are important at fast strain rates between ~450-700 °C, and show a
45
46 systematic trend with increasing temperature of recrystallisation altering from
47
48 BLG to SGR and finally GBM, although the onset temperature of each
49
50 process will be affected by other variables such as strain rate and percent
51
52 shortening.
53
54
55
56
57
58
59
60
61
62
63
64
65

4.3. Recrystallisation and Crystal-Plastic Deformation

All of the experimental runs, with the exception of 032 (450 °C), contain evidence for crystal-plastic deformation by dislocation creep evident through the development of low-angle ($\sim 2^\circ$) sub-grain boundaries (Fig. 8) (Barrie et al., 2007). As temperature of experimental deformation increases from 450 °C to 700 °C, there is a systematic change in abundance and distribution of low-angle dislocation walls (Fig. 7, 8). The undeformed starting pyrite ore material (B-1) contains few low-angle dislocation walls and the low-angle ($\sim 2^\circ$) peak in the neighbour-pair (correlated) misorientation histogram is minimal (Fig. 7). The lowest temperature run, 032 (450 °C), also contains few low-angle ($\sim 2^\circ$) dislocation walls, but does show an increased low-angle, neighbour-pair peak compared to the starting material (Fig. 7).

Between 470 °C and 550 °C, low-angle ($\sim 2^\circ$) sub-grain boundaries increase systematically (Fig 7, 8). However, low-angle boundaries start to decrease in abundance at 650 °C and by 700 °C they are generally restricted to pyrite-pyrite grain boundaries and are minimal (Fig. 7, 8). This trend is mimicked by the graphs for mean cumulative lattice misorientation (distortion) within the experimental runs (Table 1; Fig. 9), with internal distortion increasing between 450 °C to 550 °C before decreasing at 600 °C ($2 \times 10^{-5} \text{ s}^{-1}$) and ultimately dropping to levels similar to the starting material at 700 °C (Fig. 9).

The wide distribution in some of the plots (Fig. 9C, D) reflects a lower mean misorientation within the 600-650 °C samples deformed at $2 \times 10^{-5} \text{ s}^{-1}$ compared with those deformed at $2 \times 10^{-4} \text{ s}^{-1}$ (Fig. 6, 9). This general trend

1 was reported by Barrie et al. (2007) and was attributed to changing
2 recrystallisation and recovery processes with increasing temperature. A
3 similar trend is preserved in the samples new to this study with reduction in
4 low-angle dislocation walls at temperatures >600 °C indicative of the removal
5 of dislocations from pyrite grains by GBM at a pace faster than they can be
6 generated. This removal process, with increasing temperature, also explains
7 why low-angle boundary distribution is not uniform within individual pyrite
8 grains but instead tend to concentrate at grain boundaries in the higher
9 temperature samples (Fig. 8). In contrast the reduced dislocation-wall density
10 at 450 °C does not result from recovery processes, as with the other samples,
11 but reflects sample failure during loading, prior to onset of significant steady-
12 state flow and therefore, low-angle sub-grain boundary generation (Fig. 2).
13
14
15
16
17
18
19
20
21
22
23
24
25
26
27
28
29
30

31 FIG. 9 HERE
32
33
34
35

36 **4.4. The pyrite deformation mechanism map**

37
38 Recent pyrite studies (Freitag et al., 2004; Barrie et al., 2007; Barrie et
39 al., 2009; Barrie et al., 2010a) have suggested a number of potential issues
40 with the layout, construction and coverage of the strain rate contours and the
41 deformation mechanism fields in the current proposed pyrite deformation
42 mechanism map of McClay and Ellis (1983).
43
44
45
46
47
48
49
50
51
52

53 **4.4.1. Problems with the current pyrite deformation mechanism map**

54
55 The range of conditions at which crystal-plastic deformation operates in
56 pyrite in the current deformation mechanism map (Fig. 1) was initially defined
57
58
59
60
61
62
63
64
65

1 using the experimental results from Cox et al (1981). TEM analysis of these
2 experimental runs suggested dislocation glide dominated at fast strain rates
3
4 (10^{-4} s^{-1} - 10^{-5} s^{-1}) between 450-600 °C but was replaced by dislocation creep at
5
6 >650 °C. However, the same runs investigated using EBSD in this study and
7
8
9 Barrie et al. (2007), suggest dislocation creep is dominant between 500-700
10
11 °C rather than just above 650 °C (Fig. 7, 8, 9). EBSD studies of natural
12
13 samples also indicate crystal-plastic deformation, specifically dislocation
14
15 creep, is common in pyrite deformed at geological strain rates, potentially at
16
17 temperatures as low as ~200-260 °C (Freitag et al., 2004; Barrie et al., 2009).
18
19
20

21
22 Dislocation glide and creep are both crystal-plastic mechanisms of
23
24 deformation, whereby the lattice of minerals is deformed. Dislocation glide
25
26 operates freely within deforming crystals when dislocations can glide along
27
28 the lattice plane without becoming locked, due to 'obstacles' or 'opposite'
29
30 dislocations along the glide plane (Cox, 1987; Barrie et al., 2010a). Where
31
32 dislocation 'locking' occurs dislocation glide becomes either inhibited or
33
34 impossible. In order for deformation to continue dislocation climb must occur,
35
36 whereby the dislocation bypasses the blockage by moving into an adjacent
37
38 lattice place and forming a new, low-angle (~2) dislocation wall or sub-grain
39
40 boundary. The combination of dislocation glide and climb is what is referred to
41
42 as the process of dislocation creep (Paschier and Trouw, 2008; Cox, 1987)
43
44
45
46
47

48
49 All of the work in this study indicates crystal-plastic deformation in pyrite,
50
51 principally via dislocation creep, is prevalent over a much wider range of
52
53 temperature conditions than suggested by the existing mechanism map of
54
55 McClay and Ellis (1983) (Fig. 1).
56
57
58
59
60
61
62
63
64
65

1
2
3
4
5
6
7
8
9
10
11
12
13
14
15
16
17
18
19
20
21
22
23
24
25
26
27
28
29
30
31
32
33
34
35
As well as this difference in the range of deformation fields, grain size analysis of the experimentally deformed samples reveal a mean of $\sim 35\mu\text{m}$ (Fig. 3A). This is in contrast to the $\sim 100\mu\text{m}$ proposed by McClay and Ellis (1983) for their map, at least partially based upon the same samples (Cox et al., 1981). Grain size is an important constraint on the range of conditions at which diffusion and dislocation creep mechanisms operate (Atkinson, 1977; Frost and Ashby, 1982; Cox, 1987). Diffusion creep in particular is grain size sensitive and smaller grain size promotes this mechanism. Therefore, larger grain sizes have a much more restricted range of conditions at which diffusive mechanisms operate, thereby, favouring and expanding the range of conditions for dislocation creep (Atkinson, 1977; Rybacki and Dresen, 2004). Pyrite samples with a mean grain size of $\sim 35\mu\text{m}$ (this study) should have a smaller dislocation creep field on a deformation mechanisms map than samples with $100\mu\text{m}$ as in the current pyrite deformation mechanisms map of McClay and Ellis (1983).

36
37
38
39
40
41
42
43
44
45
46
47
48
49
50
51
52
53
54
55
56
57
58
59
60
61
62
63
64
65
Deformation mechanisms are described by flow laws, which are controlled by variables including: stress, activation energy, temperature and grain size (Atkinson, 1976; Cox, 1987). These flow laws affect the slope of strain rate contours in stress-temperature plots, for a defined grain size, varying from horizontal (dislocation glide), to inclined (dislocation creep) and almost vertical (diffusion creep) relative to the graph axes. In contrast, the strain rate contours proposed by McClay and Ellis (1983) (Fig. 1) have a variable slope not consistent within any of the defined deformation fields. This unusual, convex and occasionally irregular shape of the strain rate contours, at geological strain rates (Fig. 1) are, instead, governed by a pressure-

1 temperature-time pathway proposed from an earlier study (Rutter, 1976).
2 However, while this P-T-t pathway could result in strain rate contours with the
3 orientation suggested (McClay and Ellis, 1983) the specific effects are difficult,
4 if not impossible, to constrain, especially based upon the available data. The
5 slope of the strain rate contours in the diffusion-creep field of the map are also
6 inclined at $\sim 45^\circ$ similar to the slope for both dislocation fields (Fig. 1).
7 Diffusion creep is generally less sensitive to temperature than dislocation
8 creep so strain rate contour slope for diffusion creep should be closer to
9 vertical (Atkinson, 1977; Frost and Ashby, 1982). Clearly, significant revision
10 of this map is essential if it is to be used as a guide to pyrite deformation.
11
12
13
14
15
16
17
18
19
20
21
22
23
24
25

26 **4.4.2. A revised pyrite deformation mechanism map**

27 Using the results presented and discussed above, we have generated
28 a revised pyrite deformation mechanism map (Fig. 10), rectifying the issues
29 with the existing map (Fig. 1) of McClay and Ellis (1983). As with the previous
30 map of McClay and Ellis (1983), this revised map is based primarily upon
31 experimental data at geologically unreasonable fast strain rates ($10^{-4} - 10^{-5} \text{ s}^{-1}$)
32 and has required considerable extrapolation.
33
34
35
36
37
38
39
40
41
42
43
44
45

46 FIG. 10 HERE
47
48
49
50

51 The strain rate contours, although generated from limited experimental
52 data, no longer have an irregular appearance (compare Fig. 10 and Fig. 1)
53 and have been calculated using the dislocation creep flow law (Fig. 11).
54 Generating strain rate contours for this revised map was, nevertheless,
55
56
57
58
59
60
61
62
63
64
65

1 problematic, due to both scarcity of available experimental data (Cox et al.,
2 1981) and variability in stresses defining steady-state flow in the experimental
3 runs due to strain-softening (Fig. 2). This issue is insurmountable at the
4 present time, as no new, successful, pyrite deformation experiments have
5 been carried out and results published since the 1980s (Cox et al., 1981; Graf
6 et al., 1981; Cox, 1987).

7
8
9
10
11
12
13
14 A tentative flow law is proposed which uses the available mechanical
15 data, and this was used to draw the strain-rate contours for the revised
16 deformation mechanism map. The deformation fields in the map, however,
17 have been constrained using EBSD results from a spread of natural and
18 experimentally deformed pyrite-rich samples allowing greater control of the
19 conditions at which different deformation mechanisms operate, particularly
20 dislocation creep.

21
22
23
24
25
26
27
28
29
30
31
32
33
34 FIG. 11 HERE
35
36
37

38 39 **4.4.3. Strain rate contours**

40
41 Strain-rate contours on a deformation mechanism map are drawn by
42 calculating the strain-rate as a function of the two variables plotted on the
43 ordinate and abscissa. To calculate these values and extrapolate beyond the
44 experimental conditions, a flow law of the form:
45
46
47
48
49

$$50 \dot{\varepsilon} = A \sigma^n \exp\left(\frac{-Q}{RT}\right) \quad (1)$$

51
52 where $\dot{\varepsilon}$ is the strain-rate, A is the pre-exponent, σ is the stress, Q is
53
54
55
56
57
58 the activation energy, R is the gas constant, T is the absolute temperature,
59
60
61
62
63
64
65

1 must be fitted to the data. The stress exponent, n , is calculated by plotting
 2 steady state flow stress against the strain rate for constant temperature (Fig.
 3 11A). However, many of the experiments considered here failed to achieve
 4 steady-state due to continued strain softening right up to sample failure. The
 5 most reliable data are from higher temperature experiments (650-700 °C)
 6 where temperature dependent recovery can keep up with deformation rate
 7 (Fig. 4, 8).
 8
 9

10 In spite of not being able to calculate a precise value for the stress
 11 exponent (due to lack of steady-state data), it is possible to constrain the
 12 range of possible values of this parameter by using maximum (peak) and
 13 minimum (yield) values of stresses for the different experiments. These values
 14 are not meaningful in terms of steady-state flow, but provide bounds on the
 15 flow stress. Rearranging the conventional form of the creep law (equation 1)
 16 gives a form where n is the gradient of a straight line when strain-rate is
 17 plotted against stress:
 18
 19

$$20 \log_{10} \dot{\varepsilon} = \log_{10} A + n \log_{10} \sigma - \left(\frac{Q}{2.3RT} \right) \quad (2)$$

21 The data have been plotted in order to calculate the maximum and minimum
 22 values of n . These bounds are found by using different combinations of the
 23 maximum and minimum values of stress at for the two different strain-rates
 24 such that:
 25
 26

$$27 n_{\max} = \frac{1}{\log_{10} \sigma_{10^{-4} \min} - \log_{10} \sigma_{10^{-5} \max}} = \frac{1}{\log_{10} \left(\frac{\sigma_{10^{-4} \min}}{\sigma_{10^{-5} \max}} \right)} \quad (3)$$

28 and
 29
 30
 31
 32
 33
 34
 35
 36
 37
 38
 39
 40
 41
 42
 43
 44
 45
 46
 47
 48
 49
 50
 51
 52
 53
 54
 55
 56
 57
 58
 59
 60
 61
 62
 63
 64
 65

$$n_{\max} = \frac{1}{\log_{10} \sigma_{10^{-4} \max} - \log_{10} \sigma_{10^{-5} \min}} = \frac{1}{\log_{10} \left(\frac{\sigma_{10^{-4} \max}}{\sigma_{10^{-5} \min}} \right)} \quad (4)$$

where $\sigma_{\varepsilon \max}$ is the maximum stress at a given strain-rate.

Once n is calculated, the other parameters may be found by calculating the strain-rates for $\sigma=1$ and plotting the recalculated data on an Arrhenius plot ($\dot{\varepsilon}$ against $\frac{1}{T}$). The intercept of a line fitted to these data gives the value of A , with the gradient equal to $\frac{-Q}{2.3R}$ (Fig. 11B).

Since the recalculation of strain-rates for $\sigma=1$ involves using n , the values of A and Q subsequently calculated are a function of n . The range of n values calculated leads to a range of corresponding A and Q values. The dependence of the A and Q values on n means that one cannot be varied independently of the others. The deviation from the usual method of determining the flow law parameters based upon steady-state stresses is due to the limited availability of experimental data. Whilst we realise that the resulting flow law is imprecise, this work does constrain the parameter space potentially occupied by the flow law parameters.

The n_{\min} values for all of the stress-strain curves (550-700 °C) are between 1.6 and 4.27 while the n_{\max} values are more variable between 9.45 and -111. The latter values however, are not unexpected as due to the nature of log curves all negative values will extend along a curve to infinity. The n value calculated for 700 °C ($n=3.9$) is likely to be robust because both of these experiments achieved steady state (Fig. 2). The same is potentially true of the experiments at 650 °C but these results give an n value of 12.7 which is

1 outside the range of commonly expected stress exponents (Walker et al.
2 1990) suggesting these results are not as robust as they first appear. Using
3 the n_{\max} , n_{\min} and steady state flow value for 700°C n values of 3.9 and 9.45
4 have been used to construct sets of strain rate contours (Fig. 11C).
5
6
7
8
9

10 Since the 700°C experiments reach steady state, the n -value used for
11 the contours in the revised deformation mechanism map for pyrite is 3.9 (Fig.
12 10). The experiments, which do not reach steady state, are strain weakening
13 so it is likely that the flow stresses are towards the minimum end of the
14 estimates. Therefore, the minimum stress measurements have been used to
15 calculate Q and A . Strain-rate contours were plotted for the minimum values
16 of n , and using the corresponding values of Q and A , determined using the
17 minimum stress estimates. Also plotted were contours using the maximum
18 values of n , Q and A to show the potential variability in the data.
19
20
21
22
23
24
25
26
27
28
29
30

31 The strain rate contours generated from maximum values suggest
32 pyrite would need deformation stresses of ~1000MPa in order for crystal-
33 plastic deformation to proceed at ~300 °C and a strain rate of $\sim 10^{-12} \text{ s}^{-1}$. In
34 contrast, the strain rate contours generated from the minimum values suggest
35 a much weaker pyrite with deformation stresses of less than 100MPa required
36 for crystal-plastic deformation at ~300 °C and a strain rate of $\sim 10^{-12} \text{ s}^{-1}$ (Fig.
37 11C). The flow law and associated strain-rate contours allow extrapolation of
38 the experimental data outside the range of conditions explored. Any
39 extrapolations should be treated with caution due to the imprecise nature of
40 the flow law. However, these results have an advantage over many other
41 minerals because the deformation experiments were conducted at
42 geologically reasonable temperatures for crustal deformation.
43
44
45
46
47
48
49
50
51
52
53
54
55
56
57
58
59
60
61
62
63
64
65

1 The generic revised deformation mechanism map for pyrite presented
2 in this study (Fig. 10), uses the minimum n value, and Q and A values
3 calculated using the minimum stress estimates for construction of strain rate
4 contours as these are thought to give the best estimation of the flow law for
5 pyrite.
6
7
8
9
10

11 **4.4.4. Deformation Fields**

12 At temperatures between 500 °C and 700 °C and strain rates of 10^{-4} s^{-1}
13 and 10^{-5} s^{-1} the stresses for the strain rate contours in the revised deformation
14 mechanism map (Fig. 10) approximately correlate with those measured from
15 the experimental stress-strain curves (Fig. 2). However, at temperatures
16 between 450-470 °C the stress-strain curves for runs 032 and 049 (Fig 2),
17 record significantly lower stresses than those proposed from the revised strain
18 rate contours (Fig. 10). This difference implies that either the slope of the
19 strain rate contours changes at ~450 °C, becoming virtually horizontal,
20 indicative of a change in flow regime (Atkinson, 1976, 1977) or that the
21 samples have experienced cataclastic failure prior to onset of steady-state
22 flow. Cataclastic behaviour is evident in run 032 at 450 °C (Fig. 3) and also
23 present, but less apparent, in run 049 at 470 °C. Therefore, while it is feasible
24 that these samples represent a change from dislocation creep to glide
25 mechanisms (Atkinson, 1976, 1977), the obvious failure of 032 (Fig. 5A, B)
26 implies this zone represents the brittle-plastic transition zone at fast strain
27 rates. The difference in stresses between the map (Fig. 10) and the stress-
28 strain curves (Fig. 2) can, thus, be explained by early cataclastic failure, rather
29 than achieving dominant steady-state flow.
30
31
32
33
34
35
36
37
38
39
40
41
42
43
44
45
46
47
48
49
50
51
52
53
54
55
56
57
58
59
60
61
62
63
64
65

1 All of the samples analysed in this study and Barrie et al. (2007), at fast
2 strain rates, preserve low-angle ($\sim 2^\circ$) dislocation walls at temperatures in the
3
4 range 500-700 °C, indicating these conditions are within the dislocation-creep
5
6 field. Results from the naturally deformed samples (~ 30 -80 μm grain size)
7
8 also indicate dislocation creep is common at temperatures between ~ 260 -540
9
10 °C and geological strain rates ($\sim 10^{-8}$ s $^{-1}$ to $\sim 10^{-14}$ s $^{-1}$). These natural
11
12 temperature conditions were previously considered to be dominated by
13
14 diffusion creep mechanisms with crystal-plastic deformation at geological
15
16 strain rates considered to be absent (Fig. 1). These results also suggest the
17
18 brittle/diffusive-plastic transition zone at geological strain rates may be at
19
20 temperatures as low as ~ 200 -260 °C. We therefore propose a wider range of
21
22 temperature and strain rate conditions for the operation of dislocation creep in
23
24 polycrystalline pyrite with a grain size of $\sim 35\mu\text{m}$ (Fig. 10).
25
26
27
28
29
30

31 Diffusion creep was not recognised as a significant deformation
32
33 mechanism in any of the EBSD-based studies of deformed pyrite (natural or
34
35 experimental). However, identifying diffusion creep, as having been active
36
37 during deformation, is notoriously difficult and problematic to assess. This
38
39 difficulty arises from the fact that diffusion creep is only commonly reported as
40
41 the principal deformation mechanism in minerals based upon lack of evidence
42
43 for other deformation processes having operated. Similarly EBSD techniques
44
45 themselves are inherently biased towards processes, such as dislocation
46
47 creep, which result in crystal-lattice distortion. This may suggest, that the
48
49 techniques utilised in this study, overemphasises the role of dislocation
50
51 creep, which result in crystal-lattice distortion. This may suggest, that the
52
53 techniques utilised in this study, overemphasises the role of dislocation creep
54
55 to the potential detriment of diffusive mechanisms. However, this study does
56
57 not suggest that diffusion creep is not operating, simply that based upon the
58
59
60
61
62
63
64
65

1 abundant evidence for crystal-plastic distortion, at all of the conditions
2 investigated in this study, diffusion creep is subordinate to dislocation creep.
3
4 Diffusion creep is however, potentially the dominant mechanism at low stress
5 conditions beyond those investigated for pyrite deformation in this study (Fig.
6
7 10).
8
9

10
11 We therefore, propose a reduced range of conditions for diffusion
12 creep than McClay and Ellis (1983), although the transitional boundary
13 between diffusive and plastic mechanisms of deformation is at best highly
14 speculative (Fig. 10). As diffusion creep is principally grain size rather than
15 temperature dependent the slope of the strain rate contours within this field
16 changes from inclined (dislocation creep) to nearly vertical (diffusion creep).
17 The field defined as pressure solution in the previous deformation mechanism
18 map (Fig. 1) has been removed and this region is simply considered to
19 represent diffusive mechanisms due to the complexities of splitting this field
20 when grain boundary fluid effects are considered (Atkinson, 1976; Siemes,
21 1991).
22
23
24
25
26
27
28
29
30
31
32
33
34
35
36
37
38
39
40

41 **5. Conclusions**

42
43 Detecting crystal-plastic deformation in pyrite and other cubic and
44 opaque minerals is problematic, particularly using traditional techniques such
45 as reflected light microscopy and SEM-based BSE imaging. These techniques
46 make it uncertain as to whether there really is no evidence for crystal-plastic
47 deformation or if it has simply been missed due to the observational technique
48 used, particularly where cataclastic textures are widespread. Using OC
49 imaging and EBSD techniques on natural and experimental samples
50
51
52
53
54
55
56
57
58
59
60
61
62
63
64
65

1 demonstrates that plastic deformation is much more widespread than at first
2 apparent at both fast experimental (10^{-4} to 10^{-5} s $^{-1}$) and slower geological
3 strain rates (10^{-8} to 10^{-14} s $^{-1}$).
4
5

6
7 Recovery and recrystallisation, while apparently rare in naturally
8 deformed pyrite, is an important process in experimentally deformed pyrite at
9 strain rates of 10^{-4} s $^{-1}$ to 10^{-5} s $^{-1}$ and temperatures >470 °C. The experimental
10 runs show a systematic trend in recrystallisation with increasing temperature
11 from bulging (500-600 °C) to sub-grain rotation (600-650 °C) and finally grain
12 boundary migration (700 °C). The changing recrystallisation mechanisms
13 become much more effective with increasing temperature, such that
14 dislocation is virtually undetectable at >650 °C.
15
16
17
18
19
20
21
22
23
24
25

26 Studies of experimentally and naturally deformed pyrite samples
27 across a range of P-T, strain rate and stress conditions indicate crystal-plastic
28 deformation, via dislocation creep, is relatively common. These results
29 combined with all of the available experimental stress-strain curves have been
30 used to construct a revised deformation-mechanism map for polycrystalline
31 pyrite with a grain size of $\sim 35\mu\text{m}$. The most notable differences of this map
32 over the existing one are the wider range of conditions at which dislocation
33 creep operates and the change in strain rate contour slopes, which now fit
34 flow-law calculations.
35
36
37
38
39
40
41
42
43
44
45
46
47

48 Although the revised map (Fig. 10) better represents existing data, it
49 should still be considered a guide to deformation in pyrite, just as McClay and
50 Ellis (1983) indicated for their map. The reasons are the limited data available
51 for its construction, the errors inherent with determination of the flow law, and
52 the need for extrapolation from fast experimental strain rates to geologically
53
54
55
56
57
58
59
60
61
62
63
64
65

1 appropriate strain rates. Other factors, including: grain size distribution,
2 recrystallisation processes, matrix composition, modal abundance, stress
3 differences and strain heterogeneity can also affect pyrite behaviour and
4 should always be considered in any study.
5
6
7
8
9

10 11 **Acknowledgments**

12 Prof. Steve Cox (ANU) is thanked for providing further experimentally
13 deformed samples and the original stress-strain data used throughout this
14 study. Heinrich Siemes is thanked for providing a sample of the undeformed
15 starting material (B-1) and John Gilleece is thanked for sample preparation.
16 Steve Reddy and an anonymous reviewer are thanked for their constructive
17 comments which helped to improve this manuscript.
18
19
20
21
22
23
24
25
26
27
28
29
30

31 **Figure Captions**

32 **Table 1** Summary table of the deformation conditions and strain experienced
33 by all of the experimental runs investigated in this study and Barrie et al.
34 (2007). All of the experimental data was gathered by S.F.Cox and is either
35 initially presented in Cox et al. (1981) or to date unpublished.
36
37
38
39
40
41
42
43
44
45

46 **Fig. 1** The deformation mechanism map for polycrystalline pyrite with a grain
47 size of ~100 μm published by McClay and Ellis (1983). Strain rate contours
48 are in 10^{-n} s^{-1} and were defined using the results from Cox et al. (1981).
49
50
51
52
53
54

55 **Fig. 2** Stress-strain curves (Cox et al., 1981) for the experimentally deformed
56 pyrite samples with a confining pressure of 300 MPa and a strain rate of 2 x
57
58
59
60
61
62
63
64
65

1
2
3
4
5
6
7
8
9
10
11
12
13
14
15
16
17
18
19
20
21
22
23
24
25
26
27
28
29
30
31
32
33
34
35
36
37
38
39
40
41
42
43
44
45
46
47
48
49
50
51
52
53
54
55
56
57
58
59
60
61
62
63
64
65

10^{-5} s^{-1} (A) and $2 \times 10^{-4} \text{ s}^{-1}$ (B). Run 026 (A) was deformed at a strain rate of $1.2 \times 10^{-1} \text{ s}^{-1}$. Curves ending in a downward-pointing arrow terminated with specimen failure.

Fig. 3 A Box plots of grain size for the new experimental samples discussed in this study (all grains smaller than $20 \mu\text{m}$ removed): boxes represent 50% of the total data 'the body', limits of which are the interquartile range, the solid line within boxes is the median value. The 'whiskers' represent the extremes of the data ($3/2s$ of the interquartile range). **B** Crystal size distribution (CSD) plot showing the population density versus grain size ($>20 \mu\text{m}$) for all the low temperature experimental samples. **C** Crystal size distribution (CSD) plot showing the population density versus grain size for pyrite grains between $0.25 \mu\text{m}$ and $15 \mu\text{m}$ in size for the low temperature experimental samples.

Fig. 4 High spatial resolution band contrast maps of a selection of samples, deformed at temperatures between $470\text{-}700 \text{ }^\circ\text{C}$ with a strain rate of $2 \times 10^{-5} \text{ s}^{-1}$, indicating textural changes.

Fig. 5 A/B Orientation contrast images of run 032 ($450 \text{ }^\circ\text{C}$) highlighting the conjugate shear fractures running through the sample. **C**. Band contrast image highlighting the variable grain size and cataclastic nature of pyrite grains within the shear zones. **D**. Band contrast image of pyrite grains outside the conjugate shear zones highlighting their equant nature.

1 **Fig. 6** Cumulative percentage histograms plotting lattice misorientation within
2 individual grains against total percentage of grains within each sample. **A.** $2 \times$
3 10^{-4} s^{-1} **B.** $2 \times 10^{-5} \text{ s}^{-1}$
4
5
6
7
8
9

10 **Fig. 7** Misorientation angle distribution histograms plotting neighbour-pair
11 (correlated) and random-pair (uncorrelated) misorientations for a systematic
12 suite of the samples deformed at a strain rate of $2 \times 10^{-5} \text{ s}^{-1}$ and temperatures
13 between 450 °C and 700 °C.
14
15
16
17
18
19
20

21 **Fig. 8** Orientation contrast images (**A, C, E, G**) and band contrast maps with
22 overlain low-angle ($\sim 2^\circ$) sub-grain (dislocation wall) boundaries (**B, D, F, H**)
23 for the experimentally deformed pyrite samples at a strain rate of $2 \times 10^{-5} \text{ s}^{-1}$
24 and temperatures between 550-700 °C. Pole figures are included for each
25 map (*i, ii, iii, iv*) with lattice rotation axes (a, b) and rotation directions
26 highlighted (arrows).
27
28
29
30
31
32
33
34
35
36
37
38

39 **Fig. 9** Cumulative percentage histograms plotting total percentage of grains
40 against mean lattice misorientation for all of the experimentally deformed
41 samples discussed in this study. Each plot represents a particular
42 temperature regime of samples **A.** 450-500 °C **B.** 550 °C **C.** 600 °C **D.** 650 °C
43
44
45
46
47
48
49 **E.** 700 °C
50
51
52

53 **Fig. 10** The revised deformation mechanism map for polycrystalline pyrite
54 with a mean grain size of $\sim 35 \mu\text{m}$, constructed using EBSD data from this and
55 previous studies (Barrie et al., 2007; Barrie et al., 2009; Barrie et al., 2010a).
56
57
58
59
60
61
62
63
64
65

1 The contours on the map are strain rate in units of 10^{-n} s^{-1} and were calculated
2 using the original experimental stress-strain curves, some of which were
3 presented in Cox et al. (1981).
4
5
6
7
8

9 **Fig. 11 A.** Stress-strain curves for four of the experimental samples, indicating
10 how the maximum values for steady-state flow were measured. **B.** Graph
11 plotting strain rate at 0 log stress against $1/\text{Temperature}$ (in degrees Kelvin)
12 for all of the samples. The slopes of the best fit trend lines and the intercept of
13 both the minimum and maximum end-members have been used to calculate
14 Q (activation energy) and A (flow law constant). **C.** Strain rate contours plotted
15 using the maximum, minimum and median values of Q, A and n with a
16 constant grain size of $35\mu\text{m}$.
17
18
19
20
21
22
23
24
25
26
27
28
29
30

31 **References**

- 32
33
34 Allen, R.L., Weihed, P., Blandell, D., Crawford, T., Davidson, G., Galley, A.,
35 Gibson, H., Hannington, M., Herrington, R., Herzig, P., Large, R.,
36 Lentz, D., Valery Maslennikov, V., McCutcheon, S., Peter, J., Tornos,
37 F., 2002, Global comparisons of volcanic-associated massive sulphide
38 districts, *in* Blundell, D.J., Neubauer, F., Von Quadt, A., eds., The
39 Timing and Location of Major Ore Deposits in an Evolving Orogen:
40 Geological Society Special Publication Volume 204: London,
41 Geological Society, 13-37.
42
43 Ashby, M.F., 1972, A first report on deformation-mechanism maps: *Acta*
44 *Metallurgica* 20, 887-897.
45
46 Atkinson, B.K., 1975, Experimental deformation of polycrystalline Pyrite:
47 Effects of temperature, confining pressure, strain rate and porosity:
48 *Economic Geology* 70, 473-487.
49
50 Atkinson, B.K., 1976, Deformation mechanism maps for polycrystalline
51 galena: *Earth and Planetary Science Letters* 29, 210-218.
52
53 Atkinson, B.K., 1977, The kinetics of ore deformation: Its illustration and
54 analysis by means of deformation mechanism maps *Geologiska*
55 *Föreningens i Stockholm Förhandlingar* 99, 186-197.
56
57 Bailie, R.H., and Reid, D.L., 2005, Ore textures and possible sulphide partial
58 melting at Broken Hill, Aggeneys, South Africa I: Petrography: *South*
59 *African Journal of Geology* 108, 51-70.
60
61
62
63
64
65

- 1 Barrie, C.D., Boyle, A.P., Cook, N.J., Prior, D.J., 2010a, Deformation
2 mechanisms and textural changes in pyrite (FeS₂) in the massive
3 sulphide deposits of the Norwegian Caledonides: *Tectonophysics* 283,
4 269-286.
- 5 Barrie, C.D., Boyle, A.P., Prior, D.J., 2007, An analysis of the microstructures
6 developed in experimentally deformed polycrystalline pyrite and minor
7 sulphide phases using electron backscatter diffraction: *Journal of*
8 *Structural Geology* 29,1494-1511.
- 9 Barrie, C.D., Boyle, A.P., Cox, S.F., and Prior, D.J., 2008, Slip systems in
10 pyrite: An electron backscatter diffraction (EBSD) investigation:
11 *Mineralogical Magazine* 72, 1147-1165.
- 12 Barrie, C.D., Boyle, A.P., Salter, M., 2009, How low can you go? - Extending
13 downwards the limits of plastic deformation in pyrite: *Mineralogical*
14 *Magazine* 73, 895-913.
- 15 Barrie, C.D., Cook, N.J., Boyle, A.P., 2010b, Textural variation in the pyrite-
16 rich orebodies of the Røros district, Trondheim Region, Norway:
17 implications for pyrite deformation mechanisms: *Mineralium Deposita*
18 45, 51-68.
- 19 Bestmann, M., and Prior, D.J., 2003, Intragranular dynamic recrystallisation in
20 naturally deformed calcite marble: diffusion accomodated grain
21 boundary sliding as a result of subgrain rotation recrystallization:
22 *Journal of Structural Geology* 25, 1597-1613.
- 23 Boyle, A.P., Prior, D.J., Banham, M.H., Timms, N.E., 1998, Plastic
24 deformation of metamorphic pyrite: New evidence from electron-
25 backscatter diffraction and foreshatter orientation-contrast imaging:
26 *Mineralium Deposita* 34, 71-81.
- 27 Brown, D., and McClay, K.R., 1993, Deformation textures in pyrite from the
28 Vangorda Pb-Zn-Ag deposit, Yukon, Canada: *Mineralogical Magazine*
29 57, 55-66.
- 30 Cook, N.J., 1993, Conditions of metamorphism estimated from alteration
31 lithologies and ore at the Bleikvassli Zn-Pb-(Cu) deposit, Nordland,
32 Norway: *Norsk Geologisk Tidsskrift* 73, 226-233.
- 33 Cook, N.J., 1995, Polymetallic massive sulphide deposits at Baia Borsa, *in*
34 Pasava, J., Kribeck, B., and Zak, K., eds., *Mineral deposits- From their*
35 *origin to their environmental impacts: Proceedings of the Third Biennial*
36 *SGA meeting: Prague, A.A. Balkema* 851-854.
- 37 Cook, N.J., 1996, Mineralogy of the sulphide deposits at Sulitjelma, northern
38 Norway: *Ore Geology Reviews* 11, 303-338.
- 39 Cook, N.J., Halls, C., Boyle, A.P., 1993, Deformation and metamorphism of
40 massive sulphides at Sulitjelma, Norway: *Mineralogical Magazine* 57,
41 67-81.
- 42 Couderc, J.J., Bras, J., Fagot, M., Levade, C., 1980, Etude par microscopie
43 electronique en transmission d'echantillons de blende de diverses
44 provenances: *Bulletin de Mineralogie* 103, 547-557.
- 45 Cox, S.F., 1987, Flow mechanisms in sulphide minerals: *Ore Geology*
46 *Reviews* 2,133-171.
- 47 Cox, S.F., Etheridge, M.A., Hobbs, B.E., 1981, The experimental ductile
48 deformation of polycrystalline and single-crystal pyrite: *Economic*
49 *Geology* 76, 2105-2117.

- 1 Craig, J.R., 2001, Ore-mineral textures and the tales they tell: Canadian
2 Mineralogist 39, 937-956.
- 3 Craig, J.R., Vokes, F.M., 1993, The metamorphism of pyrite and pyritic ores:
4 an overview: Mineralogical Magazine 57, 3-18.
- 5 Craig, J.R., Vokes, F.M., and Solberg, T.N., 1998, Pyrite: physical and
6 chemical textures: Mineralium Deposita 34, 82-101.
- 7 Drury, M.R., and Humphreys, F., 1989, Effect of dynamic recrystallization on
8 the importance of grain-boundary sliding during creep: Journal of
9 Materials Science 24, 154-162.
- 10 Freitag, K., Boyle, A.P., Nelson, E., Hitzman, M., Churchill, J., Lopez-Pedrosa,
11 M., 2004, The use of electron backscatter diffraction and orientation
12 contrast imaging as tools for sulphide textural studies: Example from
13 the Greens Creek deposit (Alaska): Mineralium Deposita 39, 103-113.
- 14 Frost, H.J., Ashby, M.F., 1982, Deformation-mechanism maps: The plasticity
15 and creep of metals and ceramics, Pergamon press.
- 16 Gill, G.E., 1969, Experimental deformation and annealing of sulphides and
17 interpretation of ore textures: Economic Geology 64, 500-508.
- 18 Graf, J.L., and Skinner, B.J., 1970, Strength and deformation of pyrite and
19 pyrrhotite: Economic Geology 65, 206-215.
- 20 Graf, J.L., Skinner, B.J., Bras, J., Fagot, M., Levade, C., Couderc, J.J., 1981,
21 Transmission electron-microscopic observation of plastic-deformation
22 in experimentally deformed pyrite: Economic Geology 76, 738-742.
- 23 Gu, L.X., and McClay, K.R., 1992, Pyrite deformation in stratiform lead-zinc
24 deposits of the Canadian Cordillera: Mineralium Deposita 27, 169-181.
- 25 Hirth, G., Tullis, J., 1992, Dislocation creep regimes in quartz aggregates:
26 Journal of Structural Geology 14, 145-159.
- 27 Kuscu, I., Erler, A., 2002, Pyrite deformation textures in the deposits of the
28 Kure mining district (Kastamonu-Turkey): Kure Maden Sahasi
29 Yataklarinda Pirit Deformasyon Dokulari (Kastamonu-Turkiye) 11, 205-
30 215.
- 31 Leiss, B., Barber, D.J., 1999, Mechanisms of dynamic recrystallisation in
32 naturally deformed dolomite inferred from EBSD analyses:
33 Tectonophysics 303, 51-69.
- 34 Levade, C., Couderc, J.J., Bras, J., Fagot, M., 1982, Transmission electron-
35 microscopy study of experimentally deformed pyrite: Philosophical
36 Magazine a 46, 307-325.
- 37 Mann, S., Sparks, N.H.C., Frankel, R.B., Bazylinski, D.A., and Jannasch,
38 H.W., 1990, Biomineralization of ferromagnetic greigite (Fe₃S₄) and
39 iron pyrite (FeS₂) in a magnetotactic bacterium: Nature 343, 258-261.
- 40 Marshall, B., Gilligan, L.B., 1987, An introduction to remobilization: information
41 from ore-body geometry and experimental considerations: Ore Geology
42 Reviews 2, 87-131.
- 43 Marshall, B., and Gilligan, L.B., 1993, Remobilization, syntectonic processes
44 and massive sulfide deposits: Ore Geology Reviews 8, 39-64.
- 45 McClay, K.R., Ellis, P.G., 1983, Deformation and recrystallization of pyrite:
46 Mineralogical Magazine 47, 527-538.
- 47 Mohamed, F.A., Langdon, T.G., 1974, Deformation mechanism maps based
48 on grain size: Metallurgical Transactions 5, 2339-2345.
- 49
50
51
52
53
54
55
56
57
58
59
60
61
62
63
64
65

- 1 Nilsen, O., 1971, Sulphide mineralisation and wall-rock alteration at
2 Rødhammeren mine, Sør-Trondelag, Norway: Norsk Geologisk
3 Tidsskrift 51, 329-354.
- 4 Ohfuji, H., Boyle, A.P., Prior, D.J., Rickard, D., 2005, Structure of framboidal
5 pyrite: An electron backscatter diffraction study: American Mineralogist
6 90, 1693-1704.
- 7 Pearce, M.A., Wheeler, J., In Press, Grain growth and the lifetime of diffusion
8 creep: Geological Society, London, Special Publication – Deformation
9 Mechanisms, Rheology, & Tectonics: Microstructures, Mechanics, and
10 Anisotropy
- 11 Plimer, I.R., 1987, Remobilization in high-grade metamorphic environments:
12 Ore Geology Reviews 2, 231-245.
- 13 Prior, D.J., Boyle, A.P., Brenker, F., Cheadle, M.C., Austin, D., Lopez, G.,
14 Peruzzo, L., Potts, G.J., Reddy, S., Spiess, R., Timms, N.E., Trimby,
15 P., Wheeler, J., Zetterstrom, L., 1999, The application of electron
16 backscatter diffraction and orientation contrast imaging in the SEM to
17 textural problems in rocks: American Mineralogist 84, 1741-1759.
- 18 Prior, D.J., Trimby, P.W., Weber, U.D., Dingley, D.J., 1996, Orientation
19 contrast imaging of microstructures in rocks using foreshatter detectors
20 in the scanning electron microscope: Mineralogical Magazine 60, 859-
21 869.
- 22 Prior, D.J., Wheeler, J., Peruzzo, L., Spiess, R., and Storey, C., 2002, Some
23 garnet micro structures: an illustration of the potential of orientation
24 maps and misorientation analysis in microstructural studies: Journal of
25 Structural Geology 24, 999-1011.
- 26 Ramdohr, P., 1969, The ore minerals and their intergrowths: International
27 series of monographs on earth sciences, Pergamon Press, Oxford, p.
28 1174
- 29 Ranalli, G., 1982, Deformation maps in grain-size-stress spaces as a tool to
30 investigate mantle rheology: Physics of the Earth and Planetary
31 interiors 29, 42-50.
- 32 Rutter, E.H., 1976, The kinetics of rock deformation by pressure solution:
33 Philosophical Transactions of the Royal Society of London A283, 203-
34 219.
- 35 Rybacki, E., Dresen, G., 2004, Deformation mechanism maps for feldspar
36 rocks: Tectonophysics 382, 173-183.
- 37 Siemes, H., 1991, The importance of deformation experiments on minerals for
38 the interpretation of metamorphic ore textures: Ore Geology Reviews
39 6, 475-483.
- 40 Siemes, H., Zilles, D., Cox, S.F., Merz, P., Schafer, W., Will, G., Schaeben,
41 H., Kunze, K., 1993, Preferred orientation of experimentally deformed
42 pyrite measured by means of neutron-diffraction: Mineralogical
43 Magazine 57, 29-43.
- 44 Tsenn, M.C., and Carter, N.L., 1987, Upper limits of power law creep of rocks:
45 Tectonophysics 136, 1-26.
- 46 Urai, J.L., Means, W.D., Lister, G.S., 1986, Dynamic recrystallization of
47 minerals, *in* Hobbs, B.E., and H.C., H., eds., Mineral and Rock
48 Deformation: Laboratory Studies Geophysical Monograph 36, 161–
49 199.

- 1 Vokes, F.M., 1980, Some aspects of research into the Caledonian
2 stratabound sulphide deposits of Scandinavia: Norges Geologiske
3 Undersokelse 360, 77-93.
- 4 Walker, A.N., Rutter, E.H., and Brodie, K.H., 1990, Experimental study of
5 grain-size sensitive flow of synthetic hot-pressed calcite rocks, *In*
6 :Knipe, R.J. & Rutter, E.H. (eds) *Deformation Mechanisms, Rheology*
7 *and Tectonics*. Geological Society, London. Special Publications 54,
8 259-284.
- 9 Wheeler, J., Prior, D.J., Jiang, Z., Spiess, R., Trimby, P.W., 2001, The
10 petrological significance of misorientations between grains:
11 Contributions to Mineralogy and Petrology 141, 109-124.
- 12 White, S.H., 1976, The effects of strain on the microstructures, fabrics and
13 deformation mechanisms in quartzites: Philosophical Transactions of
14 the royal society of London A283, 69-86.
- 15
16
17
18
19
20
21
22
23
24
25
26
27
28
29
30
31
32
33
34
35
36
37
38
39
40
41
42
43
44
45
46
47
48
49
50
51
52
53
54
55
56
57
58
59
60
61
62
63
64
65

Table 1

Sample No.	Temperature	Confining P.	Strain Rate	Strain (%)
Run 032	450°C	300	$2 \times 10^{-5} \text{ s}^{-1}$	4.0%
Run 049	470°C	300	$2 \times 10^{-4} \text{ s}^{-1}$	20.0%
Run 035	500°C	300	$2 \times 10^{-5} \text{ s}^{-1}$	17.0%
Run 048	550°C	300	$2 \times 10^{-4} \text{ s}^{-1}$	34.0%
Run 026	550°C	300	$1.2 \times 10^{-1} \text{ s}^{-1}$	35.6%
Run 037	550°C	300	$2 \times 10^{-5} \text{ s}^{-1}$	29.0%
Run 092	600°C	300	$2 \times 10^{-4} \text{ s}^{-1}$	22.0%
Run 063	600°C	300	$2 \times 10^{-4} \text{ s}^{-1}$	40.5%
Run 054	600°C	300	$2 \times 10^{-5} \text{ s}^{-1}$	32.0%
Run 059	650°C	300	$2 \times 10^{-4} \text{ s}^{-1}$	40.0%
Run 055	650°C	300	$2 \times 10^{-5} \text{ s}^{-1}$	15.0%
Run 053	700°C	300	$2 \times 10^{-4} \text{ s}^{-1}$	32.0%
Run 020	700°C	300	$2 \times 10^{-5} \text{ s}^{-1}$	22.5%

Table 1

Figure 1

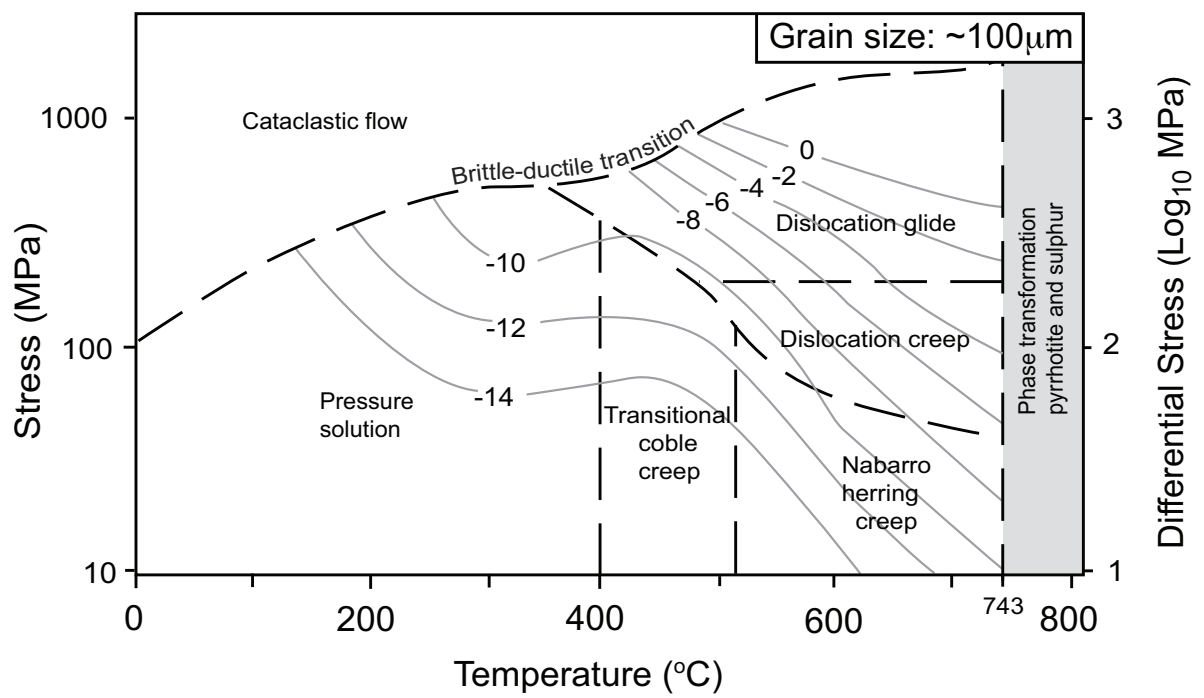


Fig. 1

Figure 2

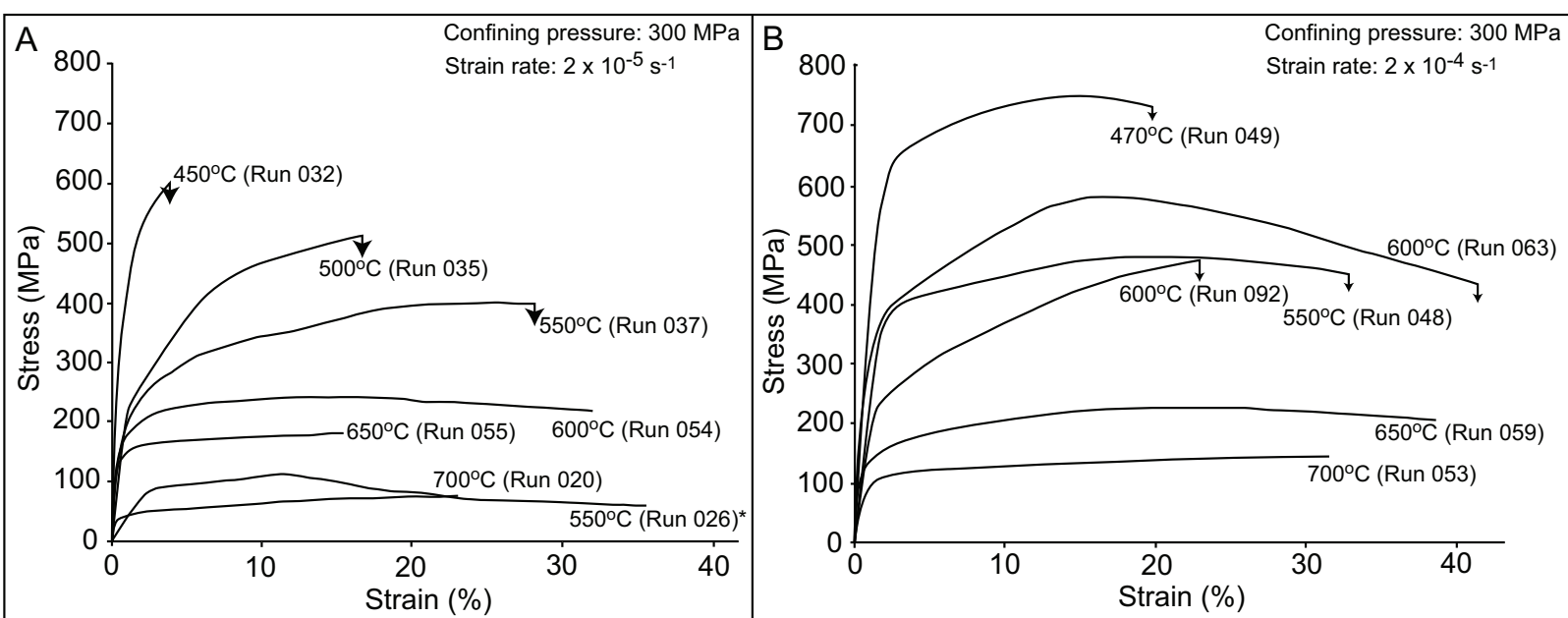


Fig. 2

Figure 3

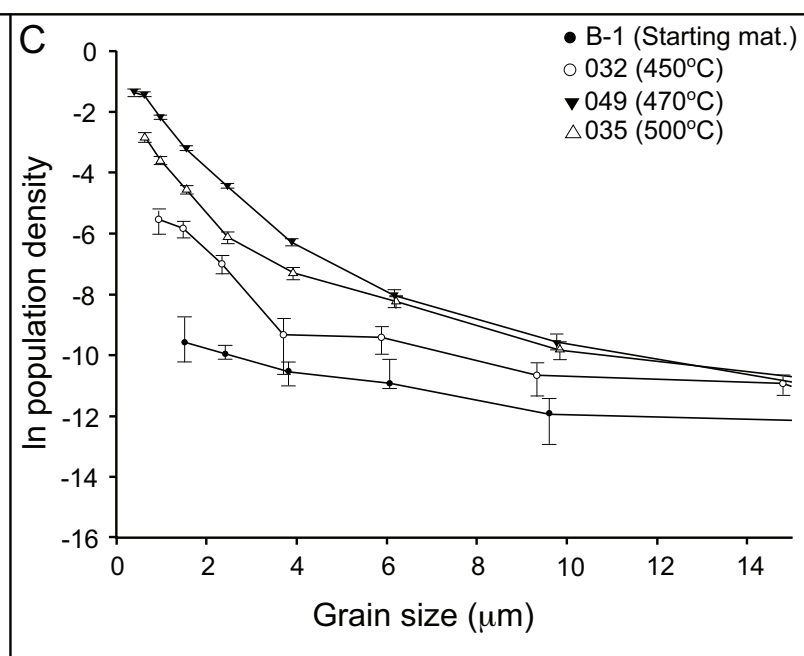
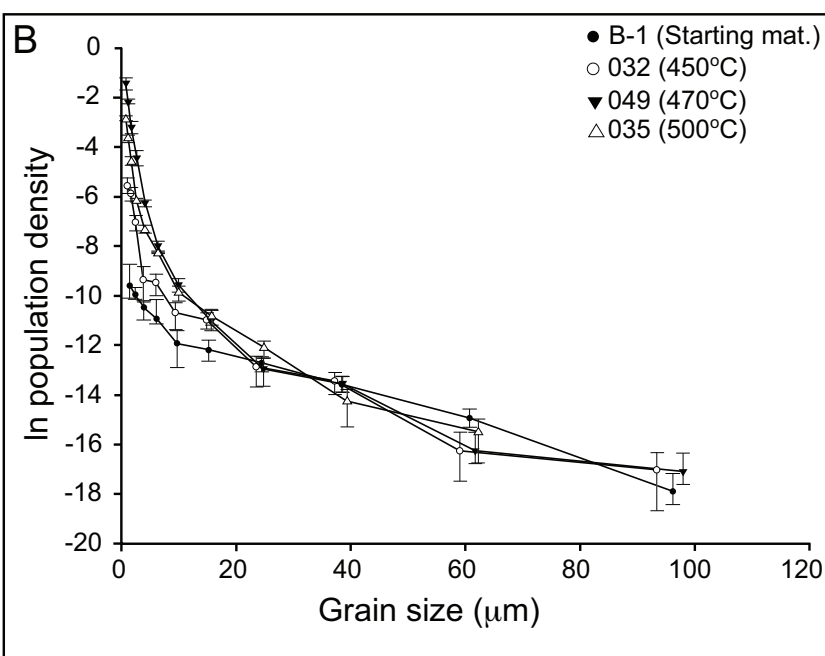
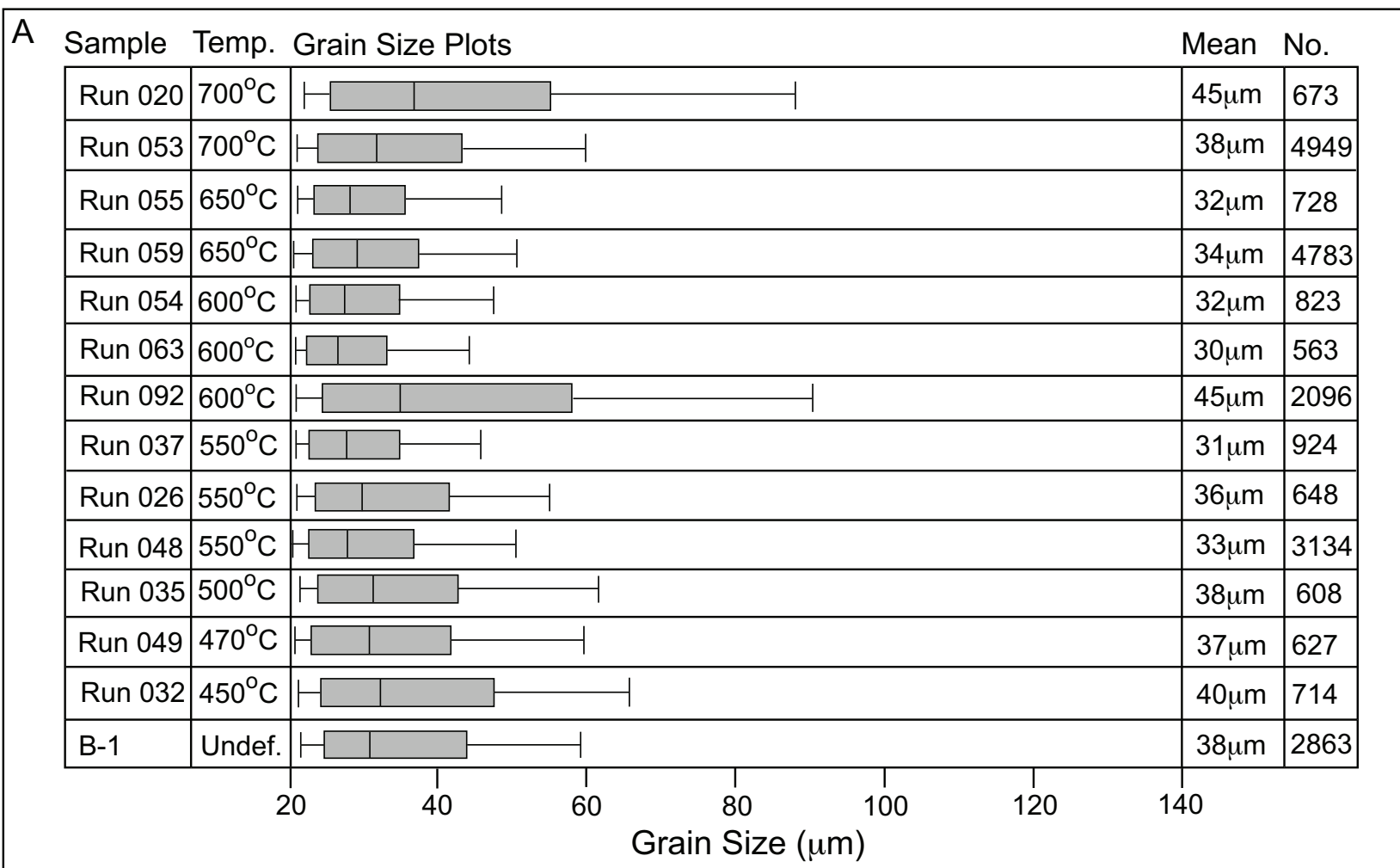


Fig. 3

Figure 4

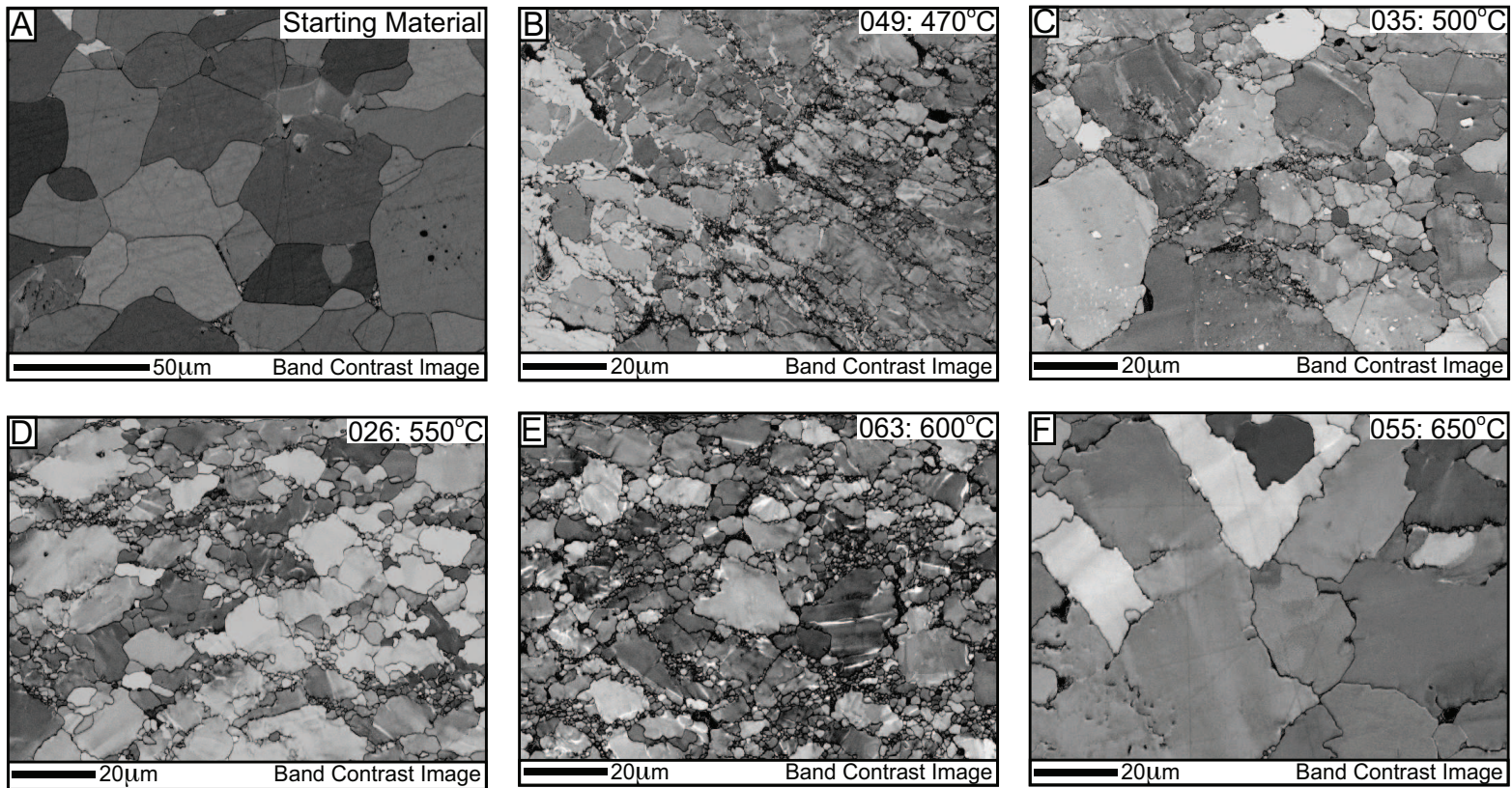


Fig. 4

Figure 5

Fig. 5

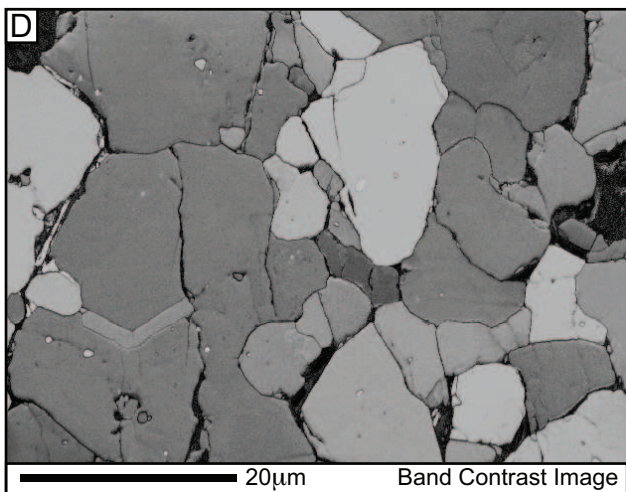
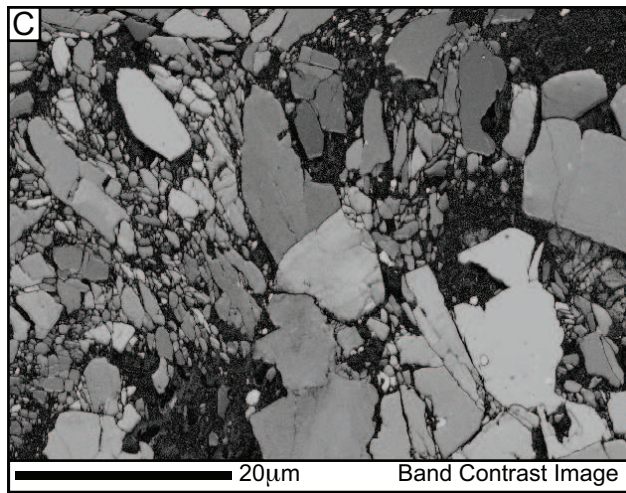
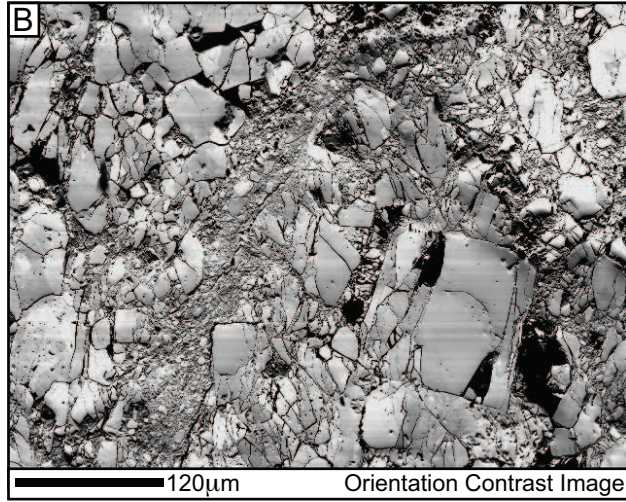
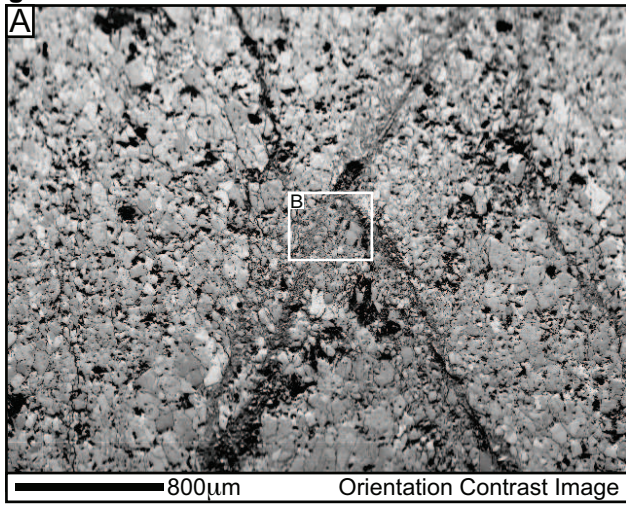


Figure 6

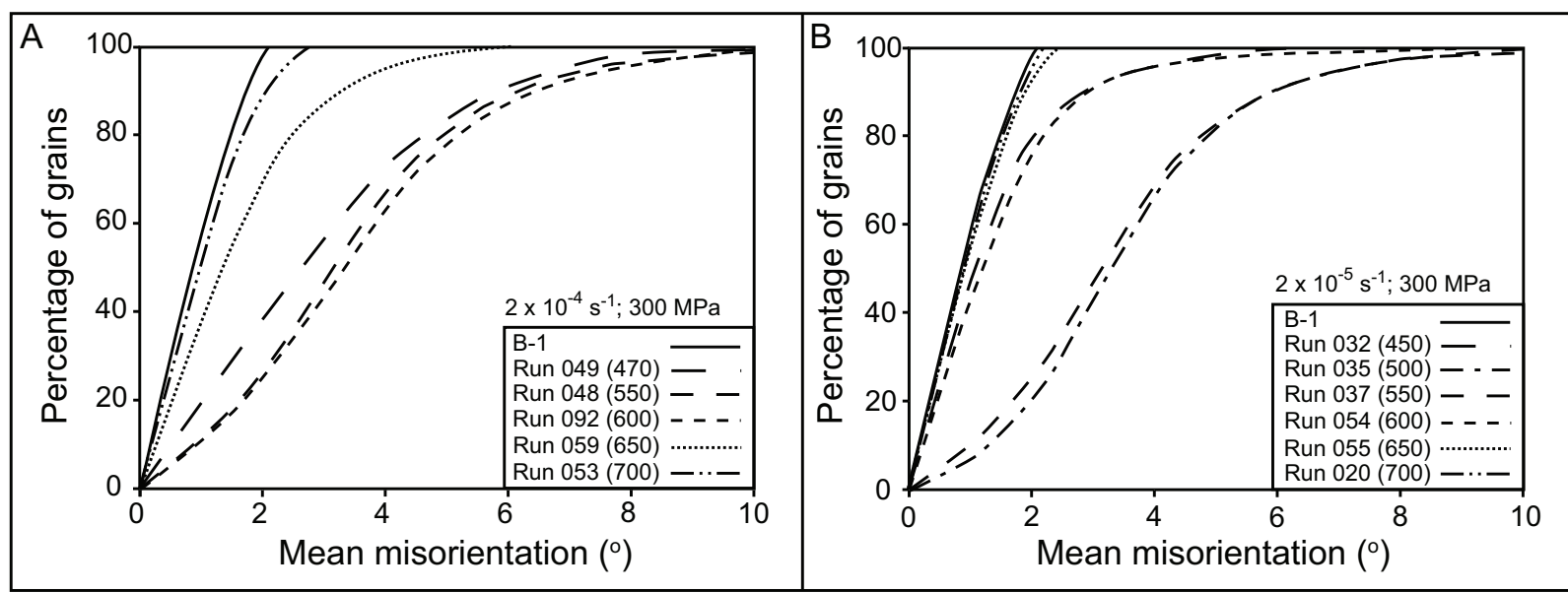


Fig. 6

Figure 7

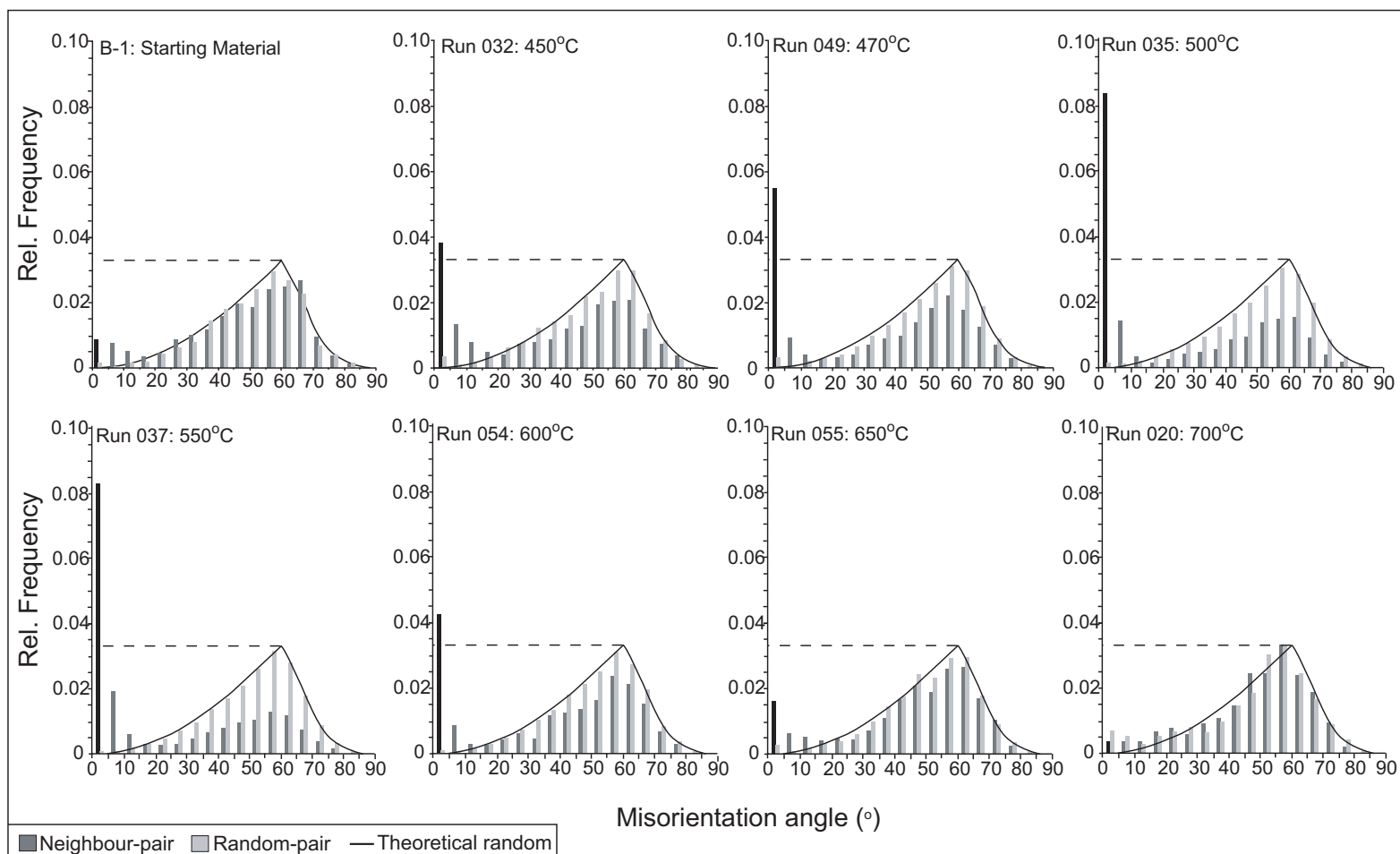


Fig. 7

Figure 8

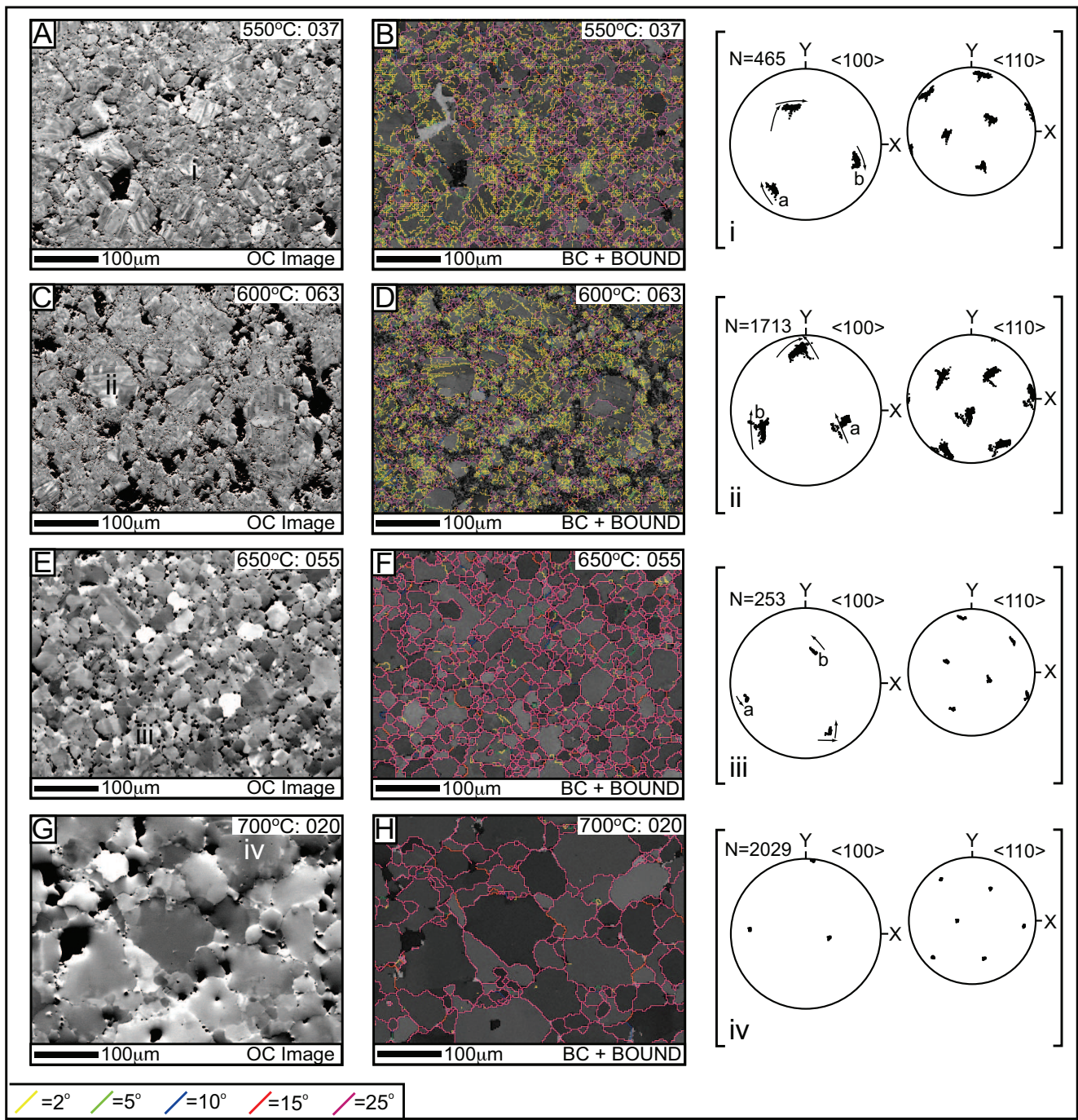


Fig. 8

Figure 9

Fig. 9

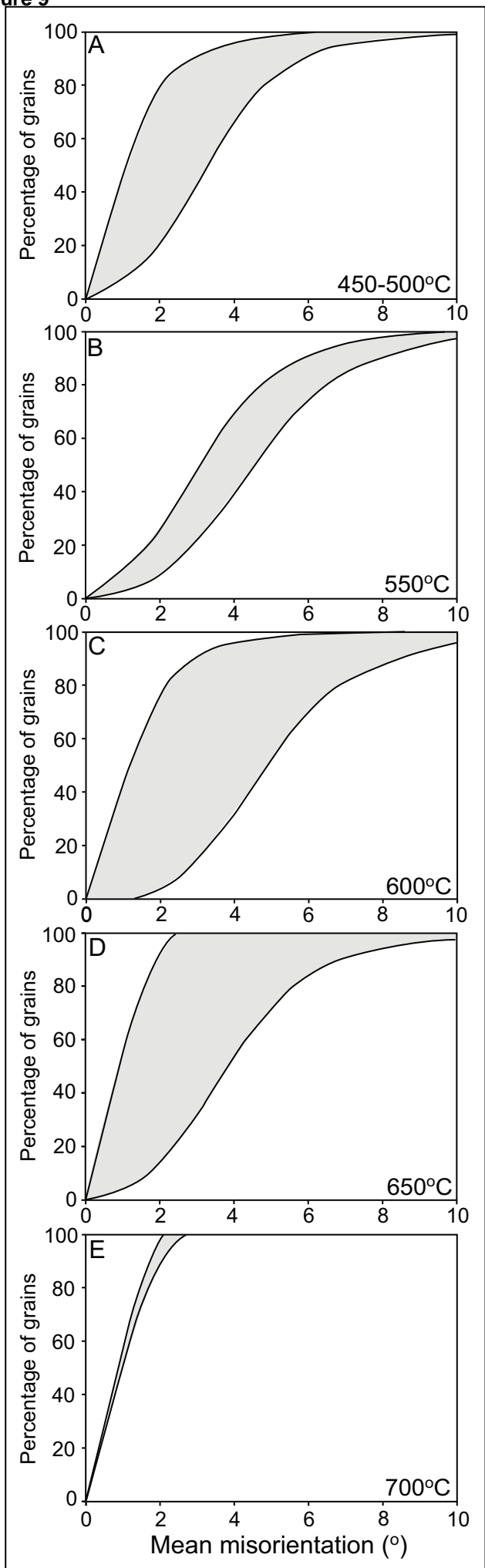


Figure 10

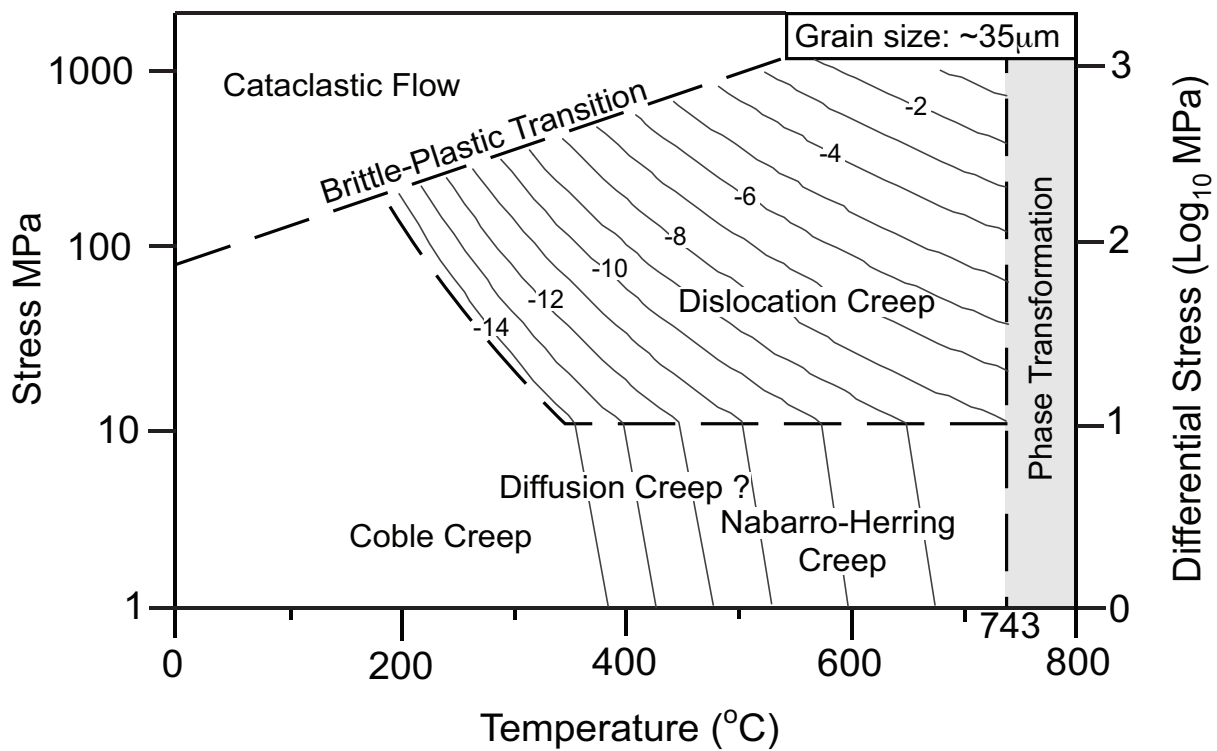


Fig. 10

Figure 11

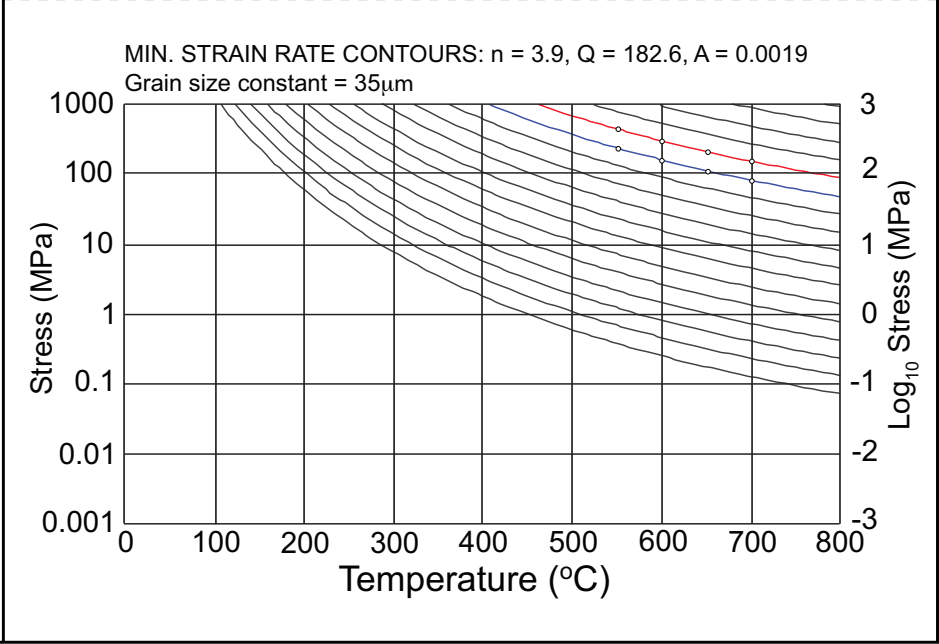
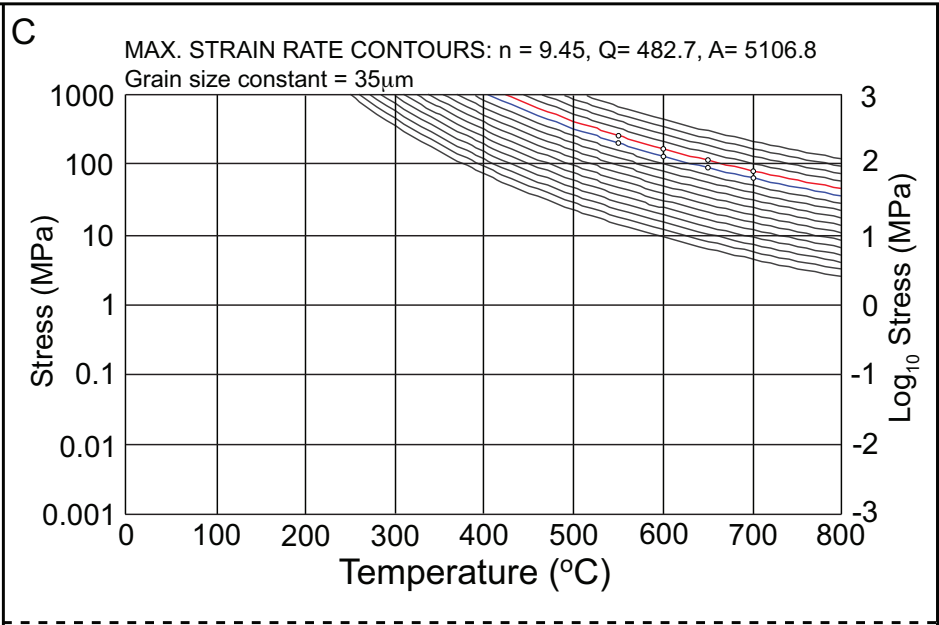
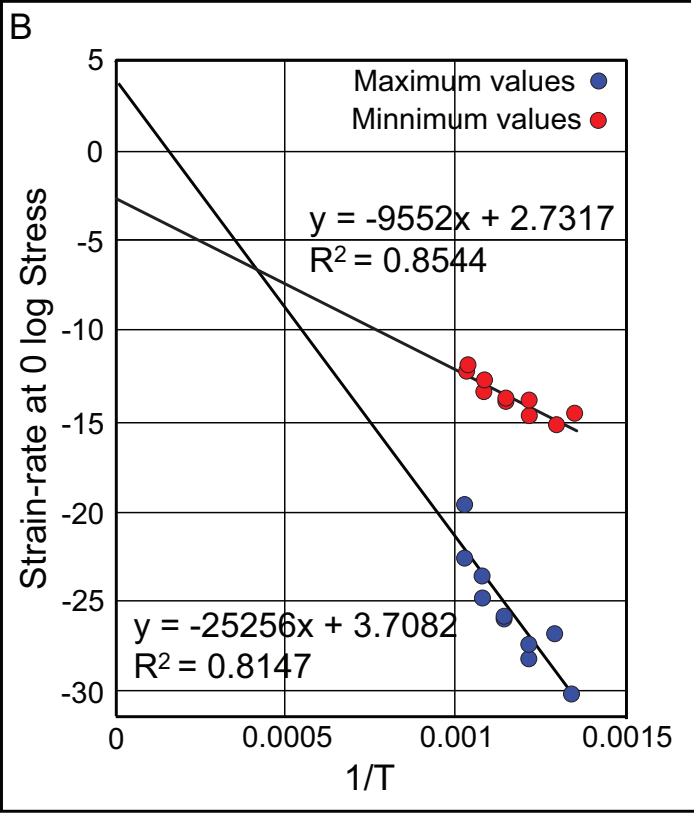
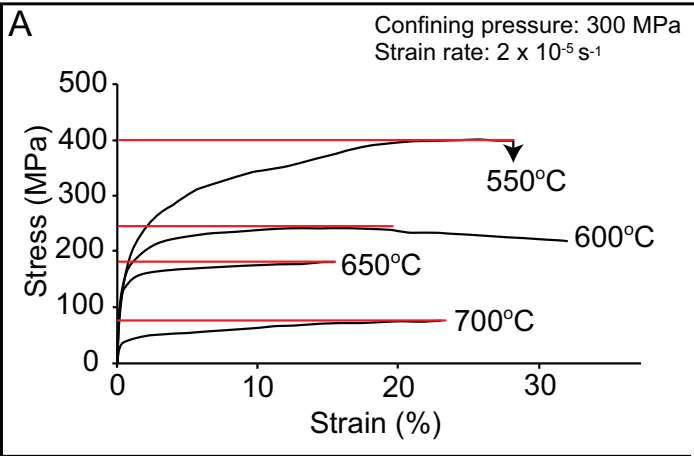


Fig. 11